Voltage- and Branch-specific Climbing Fiber Responses in Purkinje Cells

Yunliang Zang[1], Stéphane Dieudonné[2] & Erik De Schutter[1*]
[1] Computational Neuroscience Unit, Okinawa Institute of Science and Technology Graduate University, Okinawa 904-0495, Japan
[2] Inhibitory Transmission IBENS, CNRS UMR UMR8197, INSERM U1024, Ecole Normale Supérieure, 75005 Paris, France
[*]Correspondence: erik@oist.jp

Summary

Climbing fibers (CFs) provide instructive signals driving cerebellar learning. However, conflicting experimental studies have been reported about the reliability of CF mediated Ca^{2+} influx in Purkinje cell (PC) distal dendrites. Mechanisms causing the wide variation in duration and spikelet numbers of complex spikes (CSs) have not been explored systematically. Using a new experimentally validated PC model, we describe the full range of modifiability of CF responses to explain the experimental data and make new predictions. We find voltage state gates the initiation and propagation of dendritic spikes. PC dendrites exhibit inhomogeneous excitability with individual branches as computational units for CF input. Somatic CSs are regulated by voltage state, CF activation phase and instantaneous CF firing rate. Concurrent synaptic inputs can affect CSs by modulating dendritic responses in a spatially precise way. These voltage- and branch-specific CF responses will increase dendritic computational capacity and give PCs an active role in integrating CF signals.

Introduction

According to the Marr-Albus-Ito theory (Albus, 1971; Ito, 1972; Marr, 1969), climbing fiber (CF) inputs to Purkinje cells (PCs) carry movement error information and evoke cerebellar learning by depressing the strength of parallel fiber (PF) synaptic inputs. However, how PCs process error information conveyed by CF input remains elusive. Recently, the traditional description of 'all-or-none' CF responses (Eccles, 1977) has been questioned and lead to increased attention for the modulation of CF-evoked dendritic responses as global signals (Davie et al., 2008; Kitamura and Hausser, 2011; Najafi et al., 2014). Nevertheless, conflicting observations have been reported regarding the reliability of Ca^{2+} influx in distal spiny dendrites (Ohtsuki et al., 2012; Otsu et al., 2014; Zagha et al., 2010). Whether CF-evoked dendritic responses are 'global' or 'local' determines the functional role of CF input, because the spatial range of Ca^{2+} influx controls the dendritic sites undergoing synaptic plasticity and even the direction of cerebellar learning (Coesmans et al., 2004). Intrinsically, the confusion about the range of Ca^{2+} influx stems from a lack of understanding about mechanisms governing dendritic spike generation and propagation. Furthermore, whether individual branches of PC dendritic trees are homogeneously excitable has never been investigated due to technical limitations. The effect of clustered PF synaptic inputs onto PC dendrites (Wilms and Hausser, 2015) on CF-evoked dendritic responses is also unknown. The answers to these questions will determine whether the computational unit of the CF responses is entire dendritic tree or individual branches.

Somatic Complex spikes (CSs) were assumed to be a result of synaptic input current and somatic ionic currents (Schmolesky et al., 2002). Observations that dendritic spike variation plays a minimal role in evoking an extra somatic spikelet seemed to confirm this assumption (Davie et al., 2008), however, other experiments reported contrary observations (Ohtsuki et al., 2012; Otsu et al., 2014). Additionally, the somatic CS is quite variable *in vivo* (Burroughs et al., 2017; Warnaar et al., 2015) and its duration has been linked with the degree of trial-over-trail learning (Yang and Lisberger, 2014), but the mechanism causing CS variability remains unresolved. Spikelet numbers per CS correlate with preceding simple spike (SS) firing rate (SSFR) in some studies (Burroughs et al., 2017; Gilbert, 1976), but not in others (Mano, 1970; Warnaar et al., 2015). Recently, SSFR was reported to reliably reflect the proximal dendrite voltage state in mice during self-paced locomotion (Jelitai et al., 2016). Together, these correlations motivate us to ask whether an increase or decrease of SSFR (manifestation of bi-directional voltage variation) can modulate the CF-evoked somatic and dendritic responses. Similarly, contradictory correlations between CS spikelet numbers and the instantaneous CF firing rate (Burroughs et al., 2017; Maruta et al., 2007; Warnaar et al., 2015) require further examination.

To address these questions, a systematic exploration of both somatic and dendritic responses in the whole PC is required. Given the limited simultaneous recording sites by patch-clamp (Larkum et al., 2001) and the lack of direct spike information from Ca^{2+} imaging (Deneux et al., 2016), computer models can play an indispensable role. Here we have built a 'canonical' PC model that reproduces most available experimental observations instead of fitting it to a specific cell recording. We use this model to systematically explore factors that affect CF-evoked somatic and dendritic responses.

Results

Electrophysiological properties of SSs

Before using the model to make predictions, we first compare its basic properties with experimental data. Example cell recordings are shown in Fig. 1A-D to help compare SS properties between the model and experimental data. Our PC model spontaneously fires at 40 Hz in the absence of synaptic inputs or current injections (27 - 140 Hz in experiments). SSs initiate first at the axon initial segment (AIS) with an axosomatic delay of 0.12 ms (experimentally reported ~ 0.1 ms by Palmer et al. (2010)). The SS peak is -1 mV and its amplitude is 68 mV (-11 - -3 mV and 56 - 68 mV respectively in experiments). SSs have a half-amplitude duration of 0.22 ms (0.22 - 0.28 ms in experiments). The peak dv/dt of SSs is 530 mV/ms (440 - 540 mV/ms in experiments). The d^2v/dt^2 of SSs shows a biphasic increase, with the first component reflecting the contribution of axial current from the AIS and the second one reflecting the contribution of somatic Na^+ current. The peak value of d^2v/dt^2 is 6600 mV/ms^2 (5600 - 8200 mV/ms^2 in experiments).

Due to the absence of local Na^+ channels, SSs fail to invade the dendritic tree. The distance-dependent passive decay of SS amplitudes in the model matches experimental data by Ohtsuki et al. (2012)(Fig. 1E). The model also performs well in response to somatic current injections. The F-I curve falls completely within the experimentally measured range (Fig. 1F). When a large enough negative current is injected, the cell is silenced and shows a typical 'sag' response (illustrated in the inset of Fig. 1G). Both the peak and steady state of the 'sag' response are within the range

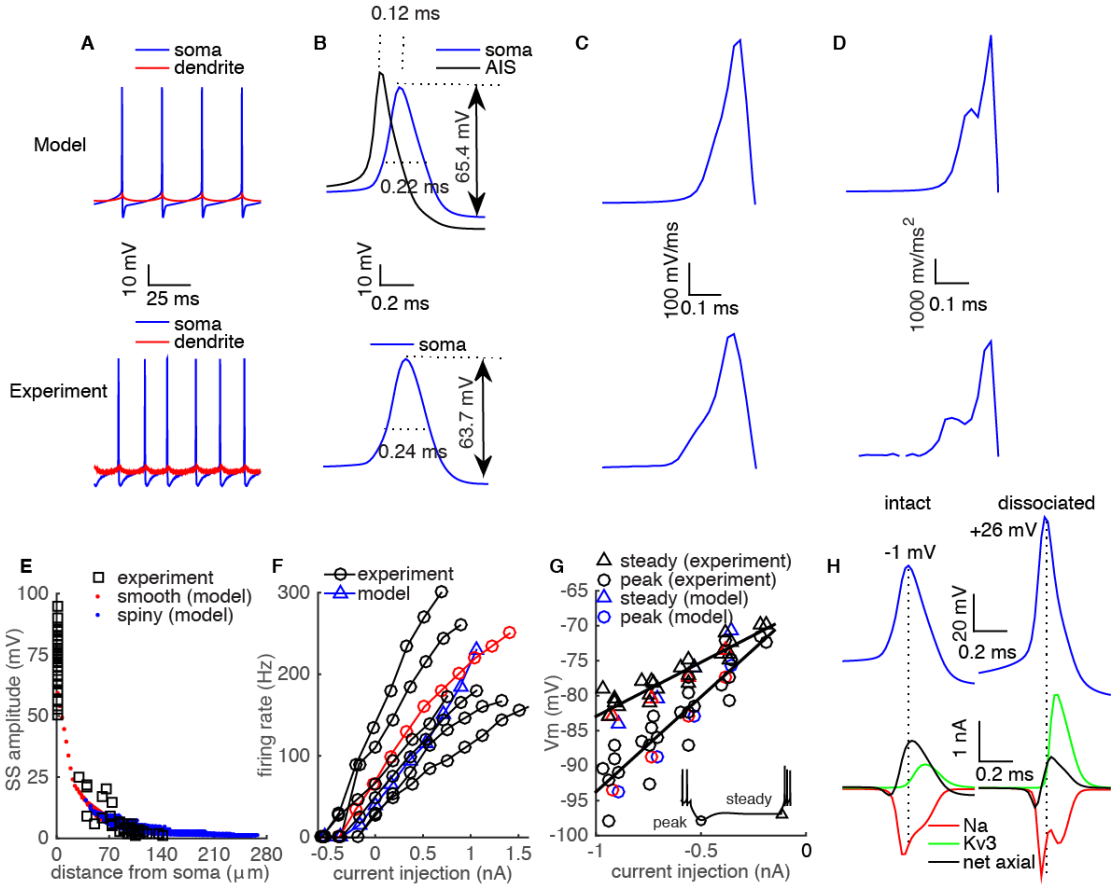

Figure 1. Model properties compare well with experimental data.
A. Spontaneously firing somatic SSs and dendritic membrane potentials (103 µm from soma) from the model (upper panel) and example experimental recording (lower panel, dendritic site is ~ 100 µm from soma). **B.** Single somatic SS waveforms from the model (upper panel) and experiment (lower panel) are shown for comparison. The spike at the AIS is shown with somatic SS to measure the axosomatic delay in the model. The *dv/dt* and d^2v/dt^2 of the somatic spike in the model (upper panel) are compared in shape and amplitude with experimental recordings (lower panel) in **C** and **D** separately. **E**, Distance-dependent decay of somatic SS amplitudes in the model and experimental recordings (data from Ohtsuki et al. (2012)). **F**, The F-I curve of the model compared with experimental recordings. Red circles represent the F-I curve of the example cell used in A-D. **G**, The peak values (the strongest hyperpolarization) and steady state values of 'sag' responses caused by negative current injections are compared between model and experimental recordings. Red symbols represent the data from the example cell used in A-D. **H**, Distinct spike (blue traces) peaks and principal ionic current profiles in intact and dissociated PCs. In the dissociated PC model, only the dendritic root section before the first bifurcation is preserved.

of experimental data (Fig. 1G) (All the preceding experimental data except Fig. 1E were shared by Ede Rancz and Michael Häusser from UCL). This good overall performance in response to current injections suggests that the model is reliable in predicting excitatory and inhibitory synaptic responses in PCs.

Dissociated PCs are often used to investigate the role of ionic currents in PC electrophysiological properties (Carter and Bean, 2009; Khaliq et al., 2003; Swensen and Bean, 2003). However, through the model, we find that the profiles of Na current (principal depolarization current (Carter and Bean, 2009)) and of Kv3 current (principal repolarization current (Martina et al., 2007)) in an intact PC differ from in a dissociated PC owing to their distinct spike properties (Fig. 1H). The SS peak in the intact PC (-1 mV) is much lower than the dissociated PC (+26 mV in the model and +32 mV in experiments by Carter and Bean (2011)). Consequently, due to their high

activation threshold (Martina et al., 2007), a much smaller fraction of Kv3 channels activate in an intact PC compared to a dissociated PC. In the intact PC, the passive dendrite repolarizes the somatic spike together with the 'less' activated Kv3 current. This large axial current (flow into dendrite) keeps pace with the somatic spike depolarization to constrain the spike peak to -1 mV (a smaller axial current exists in the dissociated PC due to the remaining dendritic stump). At the peak of the spike, the 'dip' in the Na^+ current observed in dissociated PCs (Carter and Bean, 2009) is absent in the intact PC model. The Na^+ entry ratio (defined as the ratio of total Na^+ influx to the Na^+ influx during the rising phase (Carter and Bean, 2009)) decreases from 3.1 in the dissociated PC model to 2.2 in the intact PC model. The decreased Na^+ entry ratio in the intact PC suggests that dendrites lower the metabolic cost of somatic spikes.

Generation of CF responses in the PC

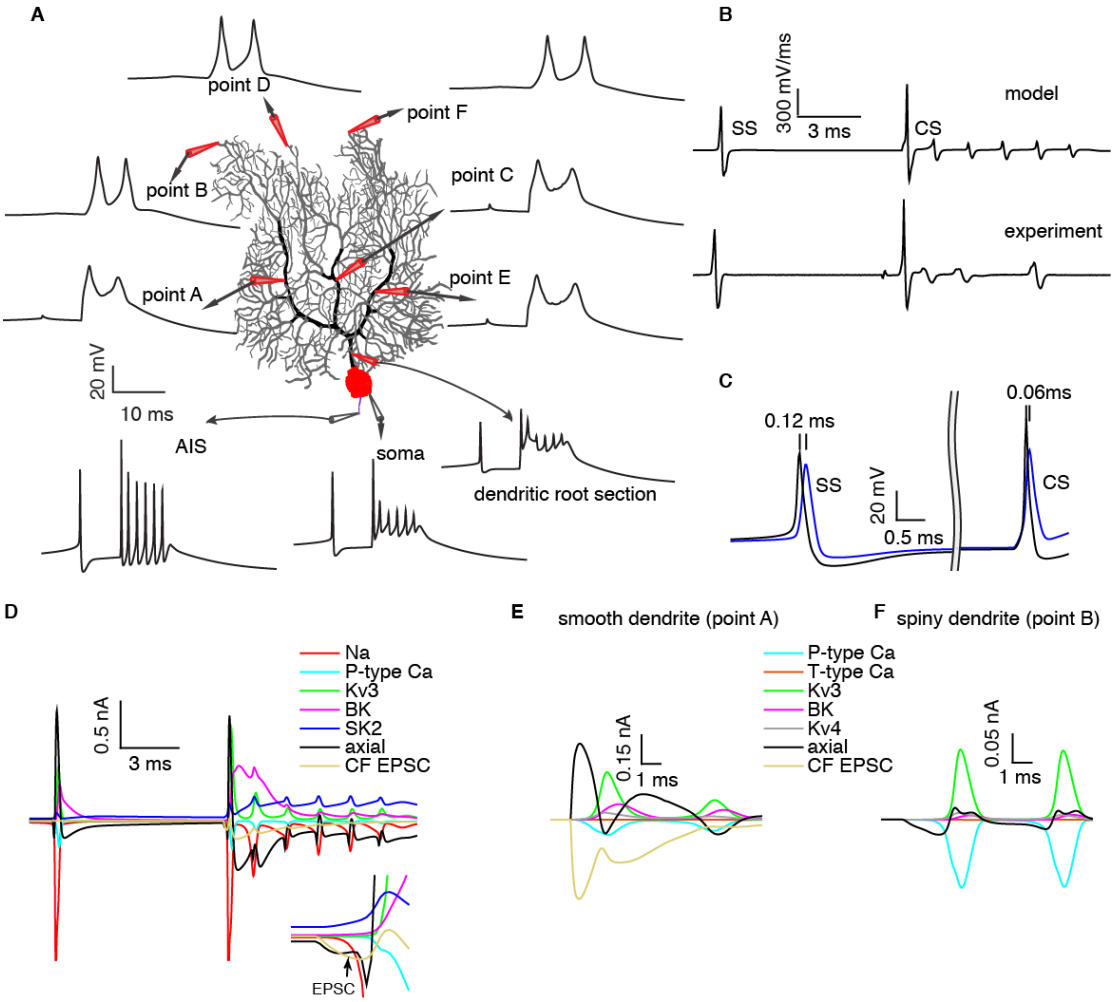

Figure 2. The generation of CF responses in the PC.
A. CF responses recorded at different sites of the PC model. Two sites on each main branch are selected as indicated in the figure. Point A (smooth dendrite) and point B (spiny dendrite) on branch 1; Point C and point D on branch 2; Point E and point F on branch 3. CF responses at dendritic root section, soma and AIS are labeled by the corresponding arrows. **B.** The peak *dv/dt* of the first spikelet in the CS increases compared with a SS in both the model (upper panel) and experiment (lower panel, the data is from Warnaar et al. (2015). **C.** The axosomatic delay of the first spikelet in the CS decreases compared with that in the SS. **D.** The composition of the somatic CS. Currents at the initial depolarization phase are enlarged in the inset. Dendritic currents at the smooth dendrite (point A) and spiny dendrite (point B) are shown in **E** and **F** in sequence. In D-F. Ionic currents are computed by multiplying the density of currents in the central segment of the corresponding section with their

surface areas (Carnevale and Hines, 2006). Surface areas of the segments chosen at the soma, smooth dendrite and spiny dendrite are 204 μm^2, 64 μm^2, and 23 μm^2, respectively. CF EPSC is absent in the spiny dendrite. Notice that different scales are used in D-F, due to different segment surface areas.

When PCs receive synaptic inputs from CFs, stereotypical somatic CSs occur at their somas. CF responses at different sites of a spontaneously firing PC model (no holding currents or background synaptic inputs) are shown in Fig. 2A. The peak *dv/dt* of the first spikelet in the CS is ~ 270 mV/ms larger than that of the SS, as confirmed by experimental data (Fig. 2B). The increased depolarization speed can facilitate the propagation of the first spikelet down to the cerebellar nuclei (CN). In the model, similar to experimental observations (Palmer et al., 2010), the CS still initiates first at the AIS. The first spikelet has an axosomatic delay of 0.06 ms, which is much shorter than that of the SS (Fig. 2C). This decreased axosomatic delay is caused by the depolarizing CF EPSC during the initial depolarization phase (Fig. 2D). The model also replicates the varied CF responses due to bursting CF input (Mathy et al., 2009) (Fig. S1).

In agreement with previous experimental findings (Swensen and Bean, 2003), the SK2 current terminates the CS (Fig. 2D). Each spikelet of the somatic CS is sharp (Fig. 2A), suggesting they are generated by Na^+ channels (Fig. 2D). Two factors determine the absence of Ca^{2+} spikes at the soma. First, the P-type Ca^{2+} current is much smaller than the Na^+ current; therefore, the Na^+ current shunts it. Second, K^+ currents are always larger than the P-type Ca^{2+} current (Fig. 2D). Magnitudes of the CF EPSC and net axial current are comparable to ionic currents at the soma (Fig. 2D), suggesting an important role in generating somatic CSs. Consequently, variation of either the CF EPSC or dendritic axial current has the potential to alter somatic CSs, as will be shown in the following sections.

The dendritic root section (the section between the soma and the first dendritic bifurcation) is electrically compact with the soma and shows mainly a passive propagation of a somatic CS. With distance from the soma, the clamping effect of a somatic CS on the dendrite weakens. The P-type Ca^{2+} current gradually dominates and cause Ca^{2+}-driven dendritic responses in the PC dendrite (Fig. 2A, E-F).

Voltage state regulates CF-evoked dendritic responses

Motivated by the variable voltage states of PCs observed *in vivo* (Jelitai et al., 2016), we systematically explore how voltage state regulates CF-evoked dendritic responses (Fig. 3). Voltage states of the PC model are manipulated by varying the somatic holding currents. Depolarization facilitates higher peaks of dendritic voltage responses with further propagation into distal spiny dendrites (Fig. 3A-C). In distal spiny dendrites, axial currents from more proximal smooth dendrites are the only current sources that can depolarize to approach the Ca^{2+} spike threshold and trigger a local dendritic spike (Fig. 3J-L). When the soma is held at -76 mV (Fig. 3A), the A-type Kv4 current is always larger than the P-type Ca^{2+} current in distal spiny dendrites (Fig. 3J). Consequently, axial currents cause only small passive depolarizations in spiny dendrites (Fig. 3D,J), and P-type Ca^{2+} channels are hardly activated (Fig. 3J). In proximal smooth dendrites, the CF provides powerful synaptic input to depolarize (Fig. 3D,M). However, this CF-evoked depolarization is still passive because the local Kv4 current and axial currents (flow into distal parts) stop the P-type Ca^{2+} current from dominating depolarization (Fig. 3M). Accordingly, the dendritic voltage responses decrease with distance from the soma in both proximal smooth dendrites and distal spiny dendrites (Fig. 3G). Distance-dependent propagation of dendritic

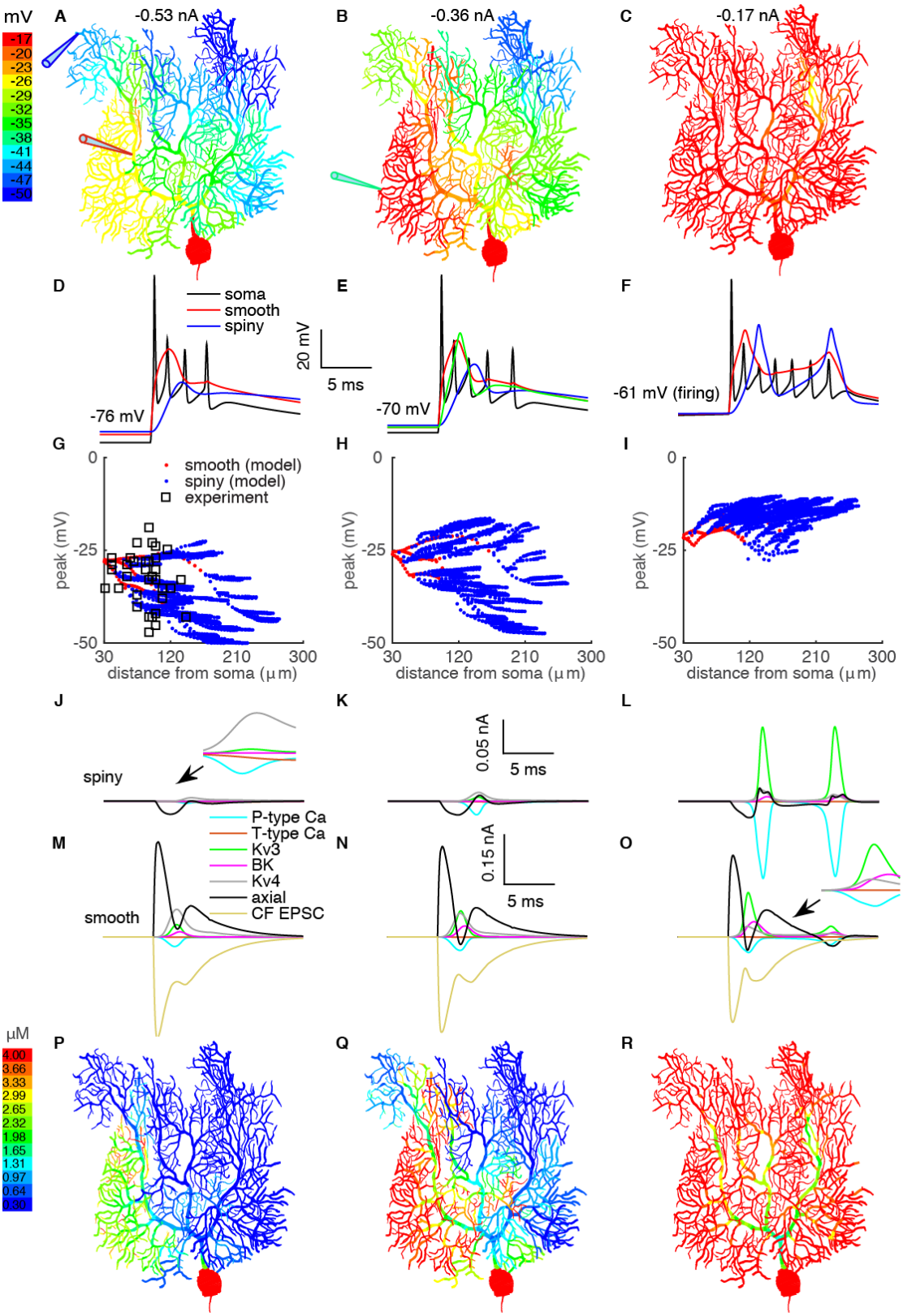

Figure 3. Voltage states regulate CF-evoked dendritic spike generation and propagation. **A-C.** Color-coded representation of dendritic voltage responses at different holding potentials (-76 mV, -70 mV and -61 mV respectively). **D-F.** Example somatic CSs (black), dendritic voltage responses on the smooth dendrite (red) and spiny dendrite (blue) at different voltage states. In **E**, an extra example dendritic voltage response (green trace, the position is labeled in B) on the spiny dendrite is shown. **G-I.** Distance-dependent propagation of dendritic responses at different voltage states. Experimental data (squares) shown in G are from Ohtsuki et al. (2012). **J-L.** Ionic currents in the distal spiny dendritic site at different voltage states. **M-O.** Ionic currents in the proximal smooth dendritic site at different

voltage states. The surface areas of the segments chosen at the smooth dendrite and spiny dendrite are 64 μm^2 and 23 μm^2 respectively. **P-R.** Color-coded peak Ca^{2+} concentrations at corresponding membrane potentials.

voltage responses matches experimental recordings under the same conditions (Ohtsuki et al., 2012) (Fig. 3G).

As the soma is held at -70 mV (Fig. 3B), dendritic spikes occur in part of the dendritic tree (the left half, proximal to the soma), where the voltage responses now increase with distance from the soma. However, the responses still decay with distance from the soma in other parts of the dendritic tree (Fig. 3B,E,H). With depolarization of the soma to -61 mV (Fig. 3C), the Kv4 current gradually inactivates and becomes smaller than the P-type Ca^{2+} current in both smooth and spiny dendrites during the initial depolarization phase (Fig. 3L,O). As a result, the P-type Ca^{2+} current depolarizes the dendrites and activates more Ca^{2+} channels in a positive feedback loop until the Kv3 current is highly activated to repolarize the spikes. Because dendritic spikes now occur globally, its peak increases with distance from the soma (Fig. 3F,I). In line with the modifiable voltage responses, the CF-evoked dendritic Ca^{2+} influx is also facilitated by the depolarization, causing larger and more widespread elevations in dendritic Ca^{2+} concentration (Fig. 3P-R). Additional CF-evoked voltage and Ca^{2+} responses at other voltage states are shown in Fig. S2.

Taken together, these results suggest that the CF-evoked Ca^{2+} influx can be gated as either a local or global signal by the voltage state of PCs. Previous seemingly conflicting observations regarding the spatial range of Ca^{2+} influx fit well with our new mechanism (Kitamura and Hausser, 2011; Najafi et al., 2014; Ohtsuki et al., 2012; Otsu et al., 2014; Zagha et al., 2010). Similarly, the discrepant dendritic spike waveforms recorded by patch-clamp from different groups can also be reconciled by distinct voltage conditions (Davie et al., 2008; Ohtsuki et al., 2012) in Fig. S3.

Inhomogeneous excitability of the dendritic tree

Dendritic spikes can occur in one part of the dendritic tree, without occurring in other parts (Fig. 3B), suggesting an asynchronous occurrence of the first spikelet at different sites of the dendrite. Similar to the first dendritic spikelet, the secondary dendritic spikelet occurs asynchronously in different branches around its threshold (Fig. 4). The secondary dendritic spikelet initially occurs at branch 1 (points A and B in Fig. 2A); then it gradually occurs at branch 2 (points C and D in Fig. 2A) and finally occurs at branch 3 (points E and F in Fig. 2A) with slight increasing depolarization. Even when secondary dendritic spikelets occur globally, their time to peak still differs between branches (Fig. 4C). Secondary dendritic spikelets peak at 8.36 ms, 10.74 ms and 13.64 ms at point A, point C and Point E respectively (relative to CF activation time). With further depolarization, secondary dendritic spikelets peak more synchronously (with 0.89 nA current injection, the respective values become 6.06 ms, 6.88 ms and 7.32 ms). The asynchronous occurrence of individual dendritic spikelets reflects the inhomogeneous excitability of each dendritic branch. In the model, the density of ionic currents is homogeneous in the spiny dendritic tree. Therefore, we investigate whether morphological differences between individual branches can account for their heterogeneity in excitability. The excitability of each branch is determined by the ratio of spiny dendrite area to smooth dendrite length in that branch (essentially the ratio of spiny dendrite capacitance load to CF synaptic input, 'load/input' ratio, see **Methods**). The 'load/input' ratios are 69, 96 and 130 at branches 1, 2 and 3 respectively, explaining their heterogeneous excitability. Moreover, within each 'big' branch, 'small' child branchlets also show heterogeneity

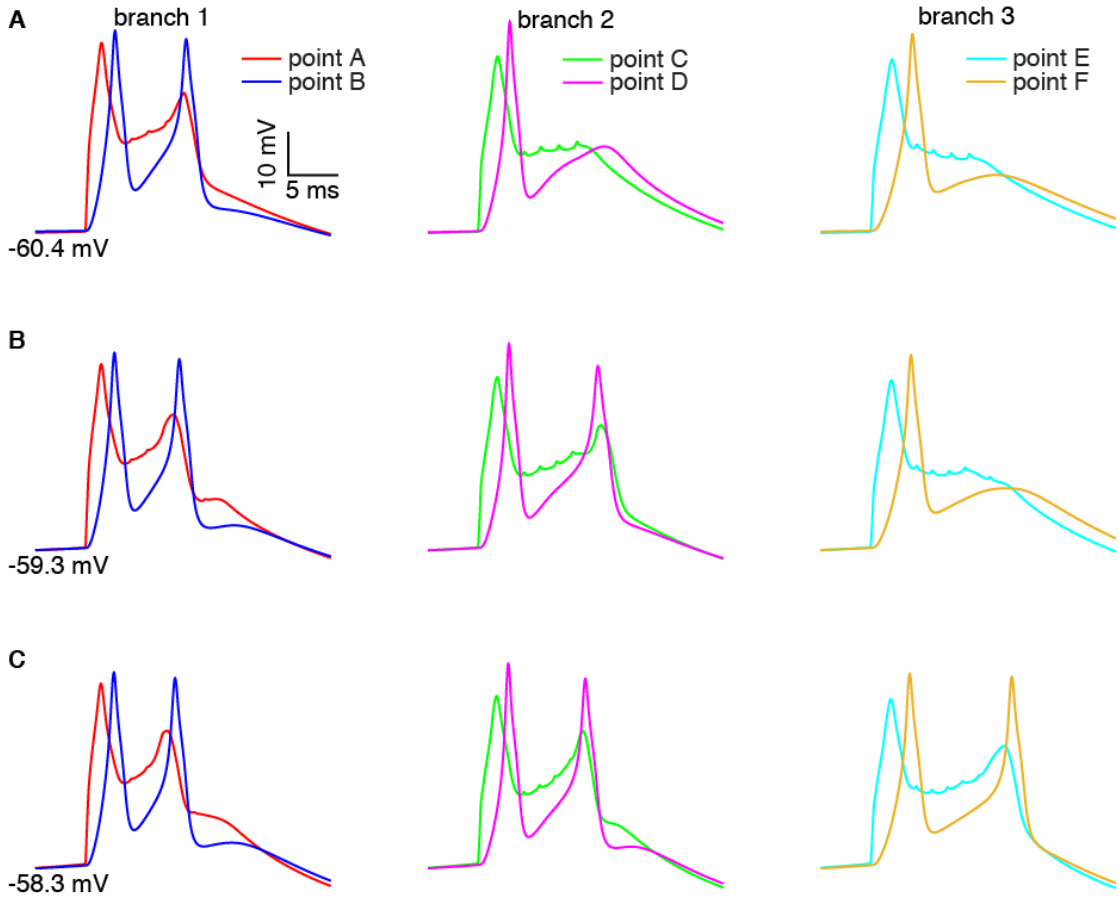

Figure 4. Branch-specific occurrence of secondary dendritic spikelets.
In all simulations, the holding current is -0.17 nA. CF input is activated at three different dendritic voltage states (different phases of somatic interspike intervals) as shown in **A**, **B**, and **C**. Points A-F are defined in Fig. 2.

in excitability, which are caused by other morphological factors such as the electrotonic distance to smooth dendrites (Fig. 3A-C).

To test the role of Kv4 current in heterogeneous dendritic excitability, we simulate the CF-evoked dendritic responses after globally decreasing its activation (left shift of the steady state availability by 11 mV). As expected, after reducing the Kv4 current, both the first and secondary dendritic spikelets occur at more hyperpolarized voltage states (Fig. S4). The whole dendrite also gets close to homogeneous at a more hyperpolarized level. Essentially the uneven distributed 'load/input' ratios underlie the heterogeneous dendritic excitability, but dendritic Kv4 channels enhance this heterogeneity.

Voltage- and phase-dependent somatic CSs

CF-evoked dendritic responses can be strongly regulated by PC voltage states. Similarly, somatic CSs also vary significantly with the depolarization of PC (Fig. 5A-C). The number of spikelets in CSs increases with initial depolarization, but decreases with further depolarization. A somatic CS results from the interaction of intrinsic ionic currents, axial current, and CF EPSC (Fig. 2D). At low voltage, although Na^+ channel availability decreases slightly (Fig. 5C), increased axial current from larger dendritic voltage responses (Fig. 5A) dominates and triggers more somatic spikelets with initial depolarization. Interestingly, the largest number of somatic spikelets coincides with the longest occurrence latency of secondary dendritic spikelets (Fig. 5A). With further depolarization, Na^+ channel availability decreases at a higher rate

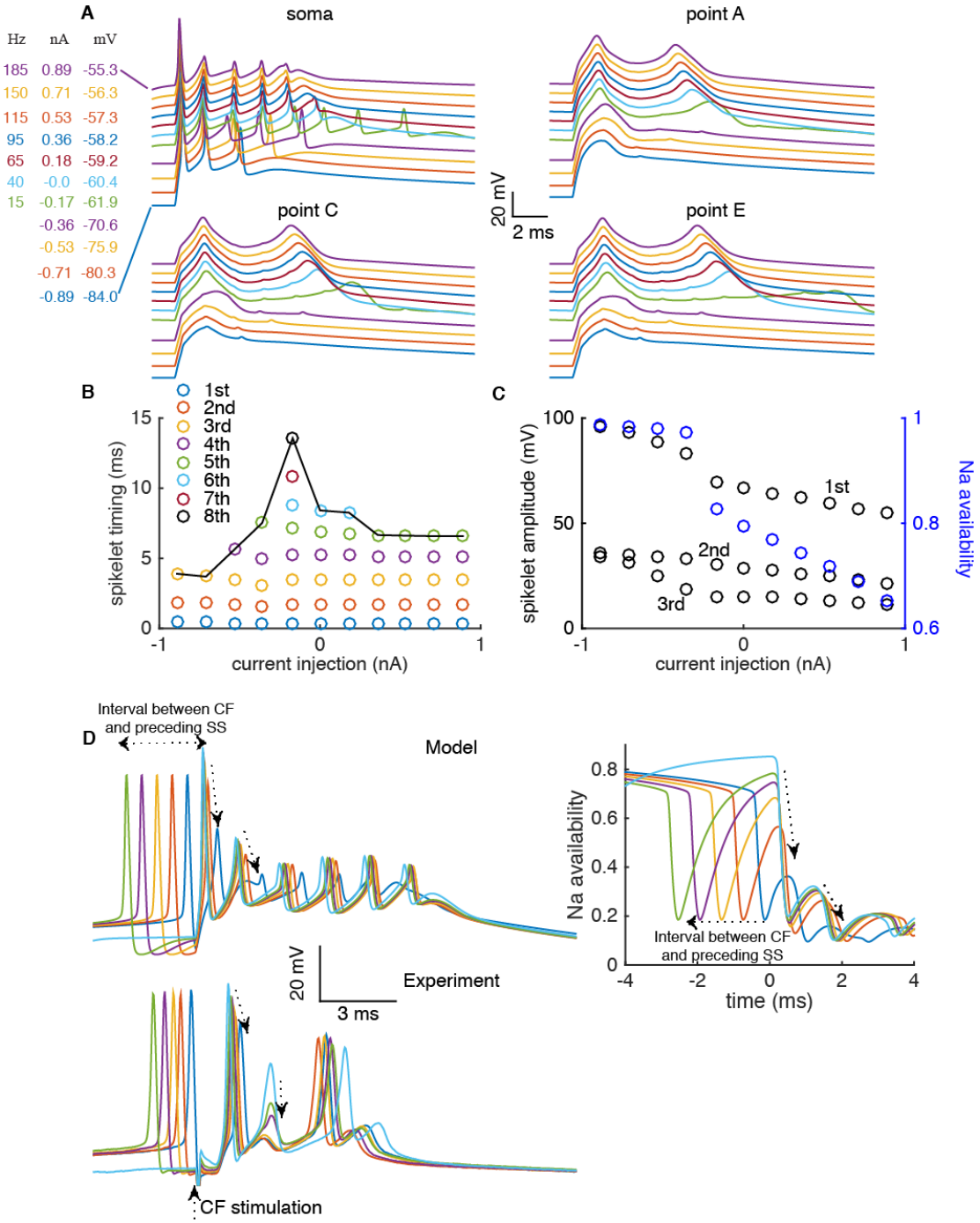

Figure 5. Voltage- and phase-dependent somatic CSs.
A. Voltage states affect somatic CSs and corresponding dendritic responses. The definition of dendritic sites is the same as in Fig. 2. The required holding currents and the firing rates at each voltage state are listed on the left. **B.** Voltage states modulate CS durations, represented by the timing of the last spikelets. **C.** In parallel with Na^+ channels availability (blue circles), amplitudes of the first three spikelets in the CS (black circles) decrease with depolarization. **D.** Amplitudes of the first and second spikelets are phase-dependent in both the model (upper left panel) and experimental recordings (lower panel). Phase-dependent recovery of Na^+ channel availability is shown in upper right panel. Experimental data are from Warnaar et al. (2015).

(Fig. 5C). Also, secondary dendritic spikelets peak much faster and closer to a preceding somatic spikelet (Fig. 5A). The shortened interval between secondary dendritic spikelets and their preceding somatic spikelet means fewer Na^+ channels are recovered to evoke an extra somatic spikelet (right axis of Fig. 5D). The critical role

of secondary dendritic spikelet timing in evoking an extra somatic spikelet agrees with previous experimental observations (Davie et al., 2008). Both factors determine the decreased somatic spikelets with further depolarization. Concurrent with spikelet numbers, CS durations are regulated by voltage states (or SSFRs), as represented by the timing of the last spikelets (Fig. 5B).

Voltage states also affect individual spikelet amplitudes in CSs. We analyzed the first three spikelets, which exist in all investigated voltage conditions. Spikelet amplitudes decrease with depolarization due to reduced availability of Na^+ channels (Fig. 5C). Individual spikelet amplitude is critical because it determines the probability of propagation down to the CN (Khaliq and Raman, 2005).

Finally, we observed phase-dependency of somatic CSs. Amplitudes of the first two spikelets in CSs decrease with shortening of the interval between the CF activation and its preceding SS (Fig. 5D). This phase-dependency reflects the time course of Na^+ channel recovery from inactivation (Fig. 5D). Subsequently, we confirmed this phase-dependency by reanalyzing *in vitro* experimental recordings (Warnaar et al., 2015), Fig. 5D).

So far, voltage states of the PC model were manipulated by varying the holding currents at the soma. We implemented further simulations, in which the net balance of excitatory PF and inhibitory synaptic inputs determines the dendritic voltage state changes, reflecting the situation *in vivo* (Jelitai et al., 2016). We find that the effect of voltage state on CF-evoked somatic and dendritic responses found *in vitro* also holds *in vivo* (Fig. S5).

Spatially constrained modulation by clustered PF/stellate cell synaptic input

Sensory stimuli can activate clustered PF synaptic inputs *in vivo* (Wilms and Hausser, 2015). Here we examine how simultaneous clustered PF or stellate cell synaptic inputs regulate CF responses. We find that clustered synaptic inputs preferentially regulate dendritic responses in a spatially constrained manner. A secondary dendritic spikelet only occurs at branch 1 with CF input in isolation (Fig. 6A). With 5 PF synapses simultaneously activated at the indicated branchlet of branch 2, the secondary dendritic spikelet also occurs at branch 2. Concurrently, an extra spikelet is evoked in the somatic CS. Nonetheless, clustered PF synaptic inputs within branch 2 do not significantly affect the dendritic responses at branches 1 and 3. Seemingly paradoxically, the extra somatic spikelet is eliminated if the number of simultaneously activated PF synapses increases to 20. As explained in the previous section, Na^+ channels need time to recover from inactivation after each somatic spikelet. Increasing the number of PF synaptic inputs accelerate the occurrence of secondary dendritic spikelets, making them occur closer to the preceding somatic spikelet, and reducing the likelihood of triggering an extra spikelet due to fewer recovered Na^+ channels. Similarly, simultaneous activation of 10 stellate cell synaptic inputs can evoke an extra somatic spikelet by delaying the occurrence of the secondary dendritic spikelet at branch 2 (Fig. 6B). Again, dendritic responses at other branches are minimally affected. The secondary dendritic spikelet still occurs in the proximal smooth dendrite even when it is eliminated in the distal part by activating 20 stellate cell synaptic inputs.

We also show that compartment-specific dendritic excitability (Ohtsuki et al., 2012), simulated here by regional Kv4 current down-regulation, modulates dendritic responses in a spatially precise way (Fig. S6).

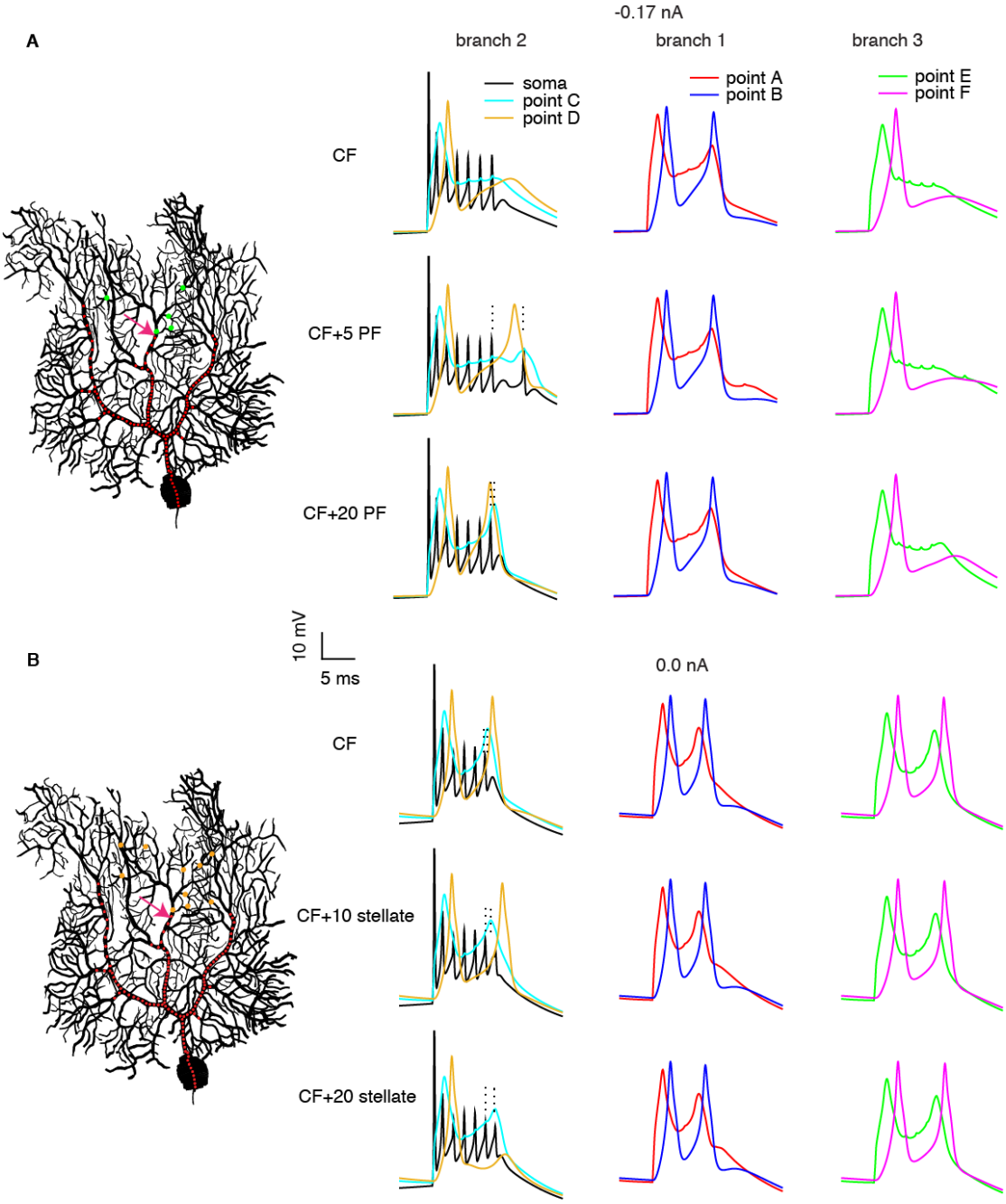

Figure 6. Simultaneous clustered PF or stellate cell synaptic input regulates the CF-evoked somatic CSs by locally modulating the dendritic responses.
A. Somatic and dendritic responses with only CF input, CF input + 5 PF synaptic inputs and CF input + 20 PF synaptic inputs are shown from top to bottom. PF synapses are randomly distributed on the child branchlet of the indicated dendritic section (green dots). **B.** Somatic and dendritic responses with only CF input, CF input + 10 stellate cell synaptic inputs and CF input + 20 stellate cell synaptic inputs are shown from top to bottom. Similar placement of stellate cell synapses (orange dots). The definition of recorded dendritic sites is the same as in Fig. 2.

Paired-pulse depression regulates CF responses in the PC

The CF activation rate can transiently reach ~ 5 - 8 Hz after sensory stimuli *in vivo* (Najafi et al., 2014; Warnaar et al., 2015). Different intervals between two consecutive CF signals (instantaneous CF firing rate) can correlate with varied spikelet numbers in CSs. However, inconsistent observations have been reported (Burroughs et al., 2017; Maruta et al., 2007; Warnaar et al., 2015) and the mechanism

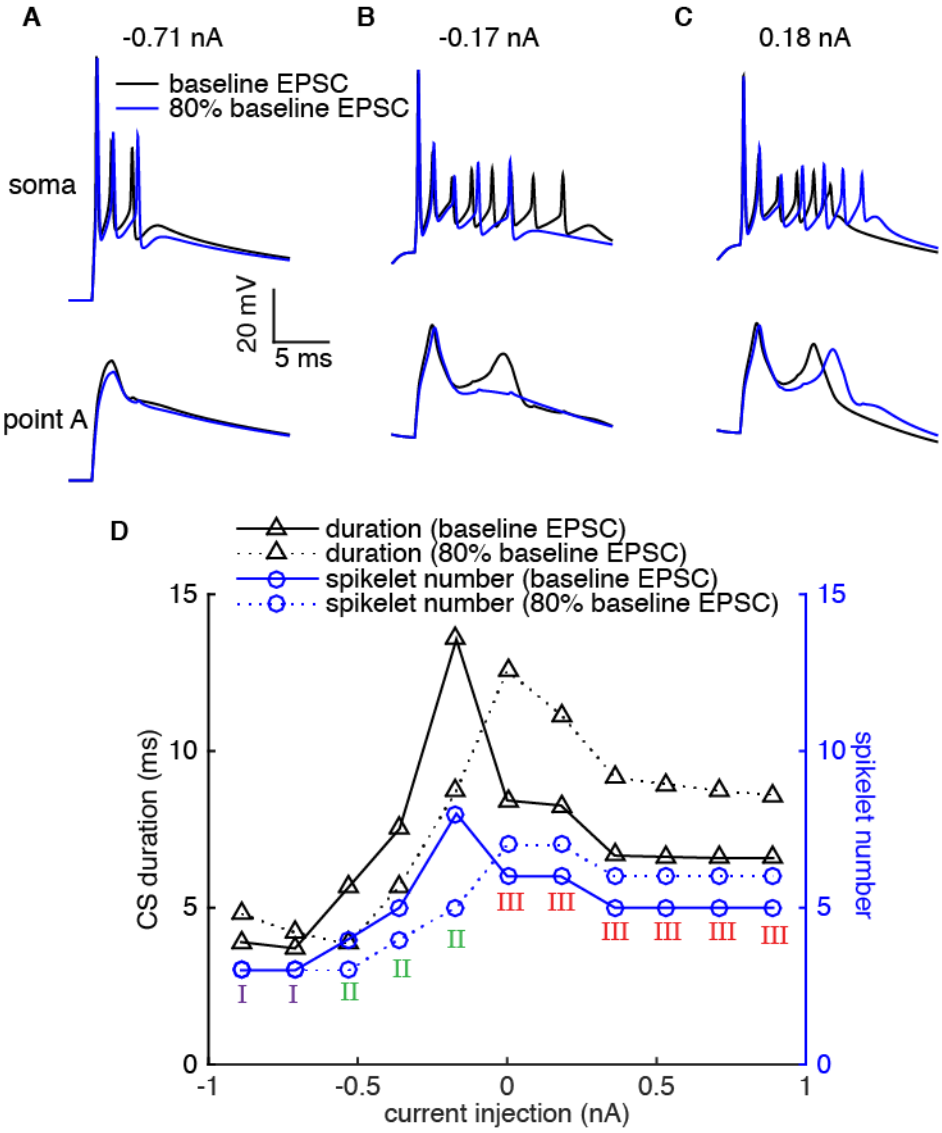

Figure 7. PPD regulates somatic and dendritic responses.
Examples of CF responses (both somatic and dendritic) with unchanged (case I), decreased (case II) and increased (case III) spikelet numbers per CS at decreased CF EPSC are shown in **A**, **B** and **C** in sequence. The effect of decreased CF EPSC on the spikelet number and duration of the CS is shown in **D**.

underpinning the correlation remains unclear. Paired-pulse depression (PPD) has been demonstrated for CF synaptic inputs *in vitro* (Andjus et al., 2005) and may be a candidate cause. To investigate the effect of PPD on CF responses, we systematically explore CF responses with baseline CF EPSC or 80% of baseline CF EPSC (~ 4 Hz of instantaneous CF firing rate in PPD experiment by Andjus et al. (2005)). We find a smaller CF EPSC consistently reduces the dendritic responses. At low voltage, the peak of the dendritic response decreases (Fig. 7A); at higher voltage, the appearance of a secondary dendritic spikelet is prevented (Fig. 7B) or delayed (Fig. 7C). The effect of PPD on the somatic CSs is more complicated. The spikelet numbers in CSs show no changes, decreases or increases with a smaller CF EPSC at different voltage states (Fig. 7A-C). A smaller CF EPSC always delays occurrence of individual somatic spikelets by providing less depolarization current. Therefore, PPD increases CS duration if the number of spikelets either does not change or increases (case I and case III in Fig. 7D). When a smaller CF EPSC evokes fewer somatic spikelets, CS

duration decreases (case II in Fig. 7D). Voltage state ranges for the occurrence of cases I-III depend on the degree of PPD. For example, when comparing with 90% of baseline CF EPSC, case I can occur at both low and high voltages (data not shown). Therefore, PPD can bridge the gap between instantaneous CF firing rates and CS variations. This new finding also reconciles the unchanged (Warnaar et al., 2015), decreased (Maruta et al., 2007), and increased (Burroughs et al., 2017) number of somatic spikelets at higher instantaneous CF firing rates (smaller CF EPSC) observed in experiments.

Discussion

We built a new PC model based on extensive experimental data to systematically investigate CF-evoked dendritic and somatic responses. Simulation results help to reveal the nature of different forms of spikes in PCs, reconcile conflicting experimental data and make new predictions. We demonstrate that CF-evoked dendritic responses are voltage-dependent and individual branches behave as computational units. Branch-specific computation can be strengthened by concurrent synaptic inputs or dendritic plasticity. We further correlate CS properties with voltage states (or SSFRs) and identify PPD as the cause of SSFR-related CS variations. Our findings offer a new perspective on how PCs dynamically process information from CF inputs.

Model accuracy

It has been demonstrated that a data set recorded from two locations in the same neuron is insufficient to accurately constrain a compartment model (Keren et al., 2005). We constrained model parameters by hand tuning and tried to replicate as many experimental observations as possible. We started by constraining somatic ionic currents based on ionic current measurements taken from dissociated PCs. These data allowed us to uniquely constrain principal somatic currents. Given the larger surface area of the soma compared to the AIS, somatic ionic currents are extremely important for PC electrophysiological properties. Subsequently, the ionic currents in the AIS and dendrites were constrained to obtain the spike properties summarized in Fig. 1. It was more difficult to constrain dendritic ionic currents due to a lack of sufficient data. The total Ca^{2+} influx during one dendritic spikelet was constrained by the experimentally estimated value (see **Supplementary Information**). In addition, the replicated CF-evoked dendritic responses under different conditions (Figs. 3,S2,S3) suggest that the dendrite model produces realistic results. Nonetheless, there is still room for improvement in the future. Due to the lack of specific data, we did not try to reproduce the role of SK2 current (Ohtsuki et al., 2012) and Kv1 current (Khavandgar et al., 2005) in regulating dendritic excitability, but such changes are not expected to affect our model predictions qualitatively.

The detailed PC model presented here follows the tradition of the biophysical modeling by De Schutter and Bower (1994a, 1994b), which has successfully predicted experimental findings (Steuber et al., 2007). Although the 1994 model is clearly outdated by recent experimental findings on PC channels, there was no suitable replacement until now. A popular PC model by Khaliq et al. (2003) has no dendrite and can therefore not be used to simulate synaptic responses. A more recent PC model (Masoli et al., 2015) has not been validated extensively against experimental data. For example, it fails to produce the stereotypical ‘sag’ responses to hyperpolarization.

Physiological predictions and implications

The model replicates spiking properties of both intact and dissociated PCs in detail. This allows us to critically evaluate predictions about the metabolic cost of spiking in PCs. Generation of spikes is energetically expensive. In a cortical pyramidal neuron, ~ 400×10^6 ATP molecules are consumed to restore the Na^+ and K^+ ion gradients after each spike (Attwell and Laughlin, 2001). Carter and Bean (2009) reported that spiking is energetically less efficient in PCs compared with cortical pyramidal neurons. However, this study was performed in dissociated PCs. In our model, the intact PC has a smaller Na^+ entry ratio compared with the dissociated PC (Fig. 1H), suggesting that dendrites increase the metabolic efficiency of somatic spikes. Given the energetic cost of spikes, it will be interesting to explore whether this dendritic role also applies to other neurons in future work.

This model allows us to systematically explore the origin of spikes observed at different parts of a PC and how they can be modulated. Dendritic spikes and somatic CSs are generated by different channels intrinsically, but they communicate via the axial currents through the dendritic root section (Fig. 2). Due to technical challenges, dendritic patch-clamp recording is usually performed on smooth dendrites of large diameter. Though we could reproduce the experiment by Davie et al. (2008) in the model (Fig. S7), we show that a single-site dendritic recording cannot reliably reflect spike occurrence and propagation in the rest of the dendritic tree. Both the peak and occurrence latency of secondary dendritic spikelets can be modulated. The peak of secondary dendritic spikelets decreases in the somatopetal direction due to unevenly distributed impedances (Roth and Hausser, 2001) and K^+ channels (Martina et al., 2003). When a secondary dendritic spikelet is 'weak', with small amplitude and long latency, it may fail to trigger a regenerative dendritic spike in the proximal dendrites (branch 1 in Fig. S7). By single-site dendritic patch-clamp, a dendritic response showing one spikelet may not correspond to a one-spikelet spike in the rest of the dendrite and therefore the role of dendritic spikes in evoking extra somatic spikelets may have been underestimated.

Our results suggest a new mechanism for PCs to process the information from CF inputs: the voltage states of PCs gate the initiation and propagation of CF-evoked dendritic responses (Fig. 3,S2,S5). This new mechanism not only reconciles the conflicting observations regarding the spatial range of CF-evoked Ca^{2+} influx (Kitamura and Hausser, 2011; Najafi et al., 2014; Ohtsuki et al., 2012; Otsu et al., 2014; Zagha et al., 2010), but also can play a functional role in regulating CF efficacy to induce plasticity in cerebellum learning. The Marr-Albus-Ito theory posits that error signals evoke CF inputs, which trigger plasticity at PF synapses (Albus, 1971; Ito, 1972; Marr, 1969). The voltage-modulated spatial range and amplitude of dendritic responses indicate that PCs may play active roles in response to error signals from CF inputs rather than passively accepting instruction from their CF 'teachers'. PF synapses can undergo not only LTD, but also long-term potentiation (LTP) (Lev-Ram et al., 2002). PF-LTD and -LTP are both Ca^{2+}-dependent, with a higher Ca^{2+} induction threshold for LTD (Coesmans et al., 2004; Piochon et al., 2016). The higher induction threshold of LTD means CF may trigger LTP instead of LTD, if the CF-evoked Ca^{2+} influx does not reach the induction threshold (Carey and Regehr, 2009; Coesmans et al., 2004). When PCs are relatively hyperpolarized, i.e. at low SSFRs *in vivo* (Jelitai et al., 2016), CF activation evokes very limited Ca^{2+} influx in the spiny dendrites and PF synapses may undergo LTP or no change instead of LTD; when PCs undergo slight depolarization, CF activation evokes dendritic spikes in only part of the distal dendrites and LTD will probably just occur in that part; when PCs are

highly depolarized (high SSFR), Ca^{2+} influx can be modulated by the number of spikelets in the dendritic spikes to affect the degree of LTD. Such effects will be further modified by stochastic gating of Ca^{2+}-activated K^{+} channels (Anwar et al., 2013), a phenomenon that was not simulated in this study.

The PC dendritic tree exhibits inhomogeneous excitability in individual branches, suggesting a computational unit at the level of individual branches, or even smaller branchlets (Fig. 4). Building upon the modulated voltage states of PCs, this new concept of branch-specific computation can undoubtedly increase the capacity of information processing in PC dendrites, in contrast to the traditionally view of the whole dendrite as the computational unit. Notably, branch-specific plasticity has already been demonstrated in other neurons such as L5 pyramidal neurons *in vitro* (Golding et al., 2002) and *in vivo* (Cichon and Gan, 2015). When PCs receive concurrent clustered synaptic input (Wilms and Hausser, 2015) or undergo localized dendritic excitability plasticity (Ohtsuki et al., 2012), CF-evoked dendritic responses can be modulated more precisely in space and magnitude to affect the plasticity induction (Fig. 6, Fig. S6).

Recently, CS durations have been linked to the degree of trial-over-trial learning in monkeys (Yang and Lisberger, 2014), with the mechanism underlying the variable CSs unresolved. The authors assumed that the variation of CS durations is due to the bursting of CF inputs, based on Mathy et al. (2009). We correlate the spikelet numbers and durations of CSs with voltage states or SSFRs (Fig. 5A-B). Besides reconciling previous contradictory correlations between spikelet numbers and SSFRs (Burroughs et al., 2017; Gilbert, 1976; Mano, 1970; Warnaar et al., 2015), our results provide an alternative interpretation of the work by Yang and Lisberger (2014). Our interpretation highlights the importance of all synaptic inputs to the PCs and resulting SSFR, not just CF, to control learning. Additionally, the CS spikelet amplitudes can be modulated by voltage states (Fig. 5C,). The timing of CF activation (phase-dependency) and concurrent synaptic input also affect somatic CSs (Fig. 5D, 6). All these factors change CS waveforms to vary the PC output and affect inhibition of the CN.

In reality, the CF input itself is not 'all-or-none' either. The variable number of spikes per CF burst can affect both somatic and dendritic responses (Mathy et al., 2009) (Fig. S1). Furthermore, CF synaptic inputs can be regulated by PPD (Andjus et al., 2005) and by norepinephrine (Carey and Regehr, 2009). Both PPD and norepinephrine can reduce the CF EPSC to modulate somatic and dendritic responses (Fig.7). In particular, PPD bridges the gap between instantaneous CF firing rates and varied CS spikelet numbers (Burroughs et al., 2017; Maruta et al., 2007; Warnaar et al., 2015) and play an important role in regulating CF responses. It is reasonable to infer that both CF inputs and PC voltage states are modulated in concert to optimize the transmission of error information down to PCs.

Conclusion

To the best of our knowledge, this study is the first to systematically explore CF responses in the PC. We believe that multiple mechanisms working synergistically to modulate CF responses will have important consequences for cerebellar learning an for signals transmitted to the CN. We hope this study will inspire experiments to directly validate modulation of CF responses *in vivo*. Special attention should be paid to PCs with low SSFRs.

Methods

All simulations were performed with NEURON, version 7.4 (Hines and Carnevale, 1997). We use the morphology of a 21-day-old Wistar rat PC (Roth and Hausser, 2001). The model consists of an axon initial segment (AIS), a soma, smooth dendrites, and spiny dendrites. The first 17 μm of the reconstructed axon are preserved as the AIS. When exploring the spike initiation site, AIS indicates the end of AIS next to the myelinated axon. The definition of other morphological parts is the same as in the original work (Roth and Hausser, 2001). The model has the following passive parameters: R_m = 120.2 kΩ cm^2, R_i = 120 Ω cm, C_m = 0.64 μF/cm^2 (Roth and Hausser, 2001). To compensate for the absence of spines in the reconstructed morphology, the conductance of passive current and C_m are scaled by a factor of 5.3 in the spiny dendrite and 1.2 in the smooth dendrite. The AIS contains Na^+ current, T-type Ca^{2+} current, P-type Ca^{2+} current, H-current, high-threshold-activated K^+ current (Kv3 current), large-conductance Ca^{2+}-activated K^+ current (BK current), and a small-conductance Ca^{2+}-activated K^+ current (SK2 current). Current distribution in the soma is similar to the AIS without the T-type Ca^{2+} current. T-type Ca^{2+} current, P-type Ca^{2+} current, H-current, Kv3 current, BK current, SK2 current, Kv1 current, and Kv4 current are distributed in both the smooth dendrite and the spiny dendrite. The conductance densities of ionic currents in corresponding parts of the model were found by hand tuning. Detailed information about ionic current equations and the process of parameter tuning can be found in the **Supplementary Information**. The source code of this model is available at ModelDB (future link).

The synaptic conductance activated by CF input is approximated as a bi-exponential waveform, with 0.3 ms and 3 ms as the rise and decay time constants (Davie et al., 2008). Unless otherwise specified, baseline peak conductance is 1.2 nS. 500 synaptic inputs are distributed on the soma and smooth dendrite at a constant density per length to simulate the CF response. The conductance varies in the range of 80% - 100% to simulate how the EPSC changes by paired-pulse depression (PPD). Due to the elaborate structure, the dendrite is not isopotential with the soma when holding current is injected at the soma. The somatic membrane potential is selected to represent the voltage state of the whole PC except in Fig. 4, in which dendritic membrane potential is used. When measuring the distance-dependence of the dendritic response peak, we selected the first dendritic spikelet if there were two spikelets. To measure excitability of individual branches, we define a new measure as the ratio of the spiny dendrite capacitance load to CF synaptic input, 'load/input' ratio, which can be transformed into 'the area of spiny dendrite'/'length of smooth dendrite' within each branch in the model. To exclude the effect of phase-dependence on CSs in Fig. 5, all the CF signals are activated with 3 ms after the preceding SS under different membrane potentials. To explore how simultaneous clustered synaptic inputs regulate dendritic response and somatic output, PF or stellate cell synaptic inputs are activated 5 ms after the CF input (Fig. 6). To simply mimic the PC voltage states *in vivo*, 1105 PF synapses and 1105 Inhibitory synapses are uniformly distributed on the spiny dendrites. Different voltage states of the PC are achieved by randomly activating excitatory and inhibitory synapses at different average firing rates.

Data availability. All the simulation data and the model code are available from the authors.

Acknowledgements

We thank Ede Rancz, Michael Häusser, Gen Ohtsuski, Christian Hansel, João Couto (the data shared by above-mentioned people were used in the manuscript for validation of the model results), Bruce Bean, Indira Raman (the data shared by above-mentioned people were used to constrain ionic current properties), Mathew Nolan, Edward Zagha and Bernardo Rudy for sharing related experimental data.

Author Contributions

Y.L.Z., S.D., and E.D.S. conceived this study; Y.L.Z. performed all the simulations; Y.L.Z. and E.D.S. analyzed the simulation data; Y.L.Z. and E.D.S. wrote the manuscript.

References

Albus, J.S. (1971). A theory of cerebellar function. Mathematical Biosciences *10*, 25-61.

Andjus, P.R., Bajic, A., Zhu, L., Schachner, M., and Strata, P. (2005). Short-term facilitation and depression in the cerebellum: some observations on wild-type and mutant rodents deficient in the extracellular matrix molecule tenascin C. Annals of the New York Academy of Sciences *1048*, 185-197.

Anwar, H., Hepburn, I., Nedelescu, H., Chen, W., and De Schutter, E. (2013). Stochastic calcium mechanisms cause dendritic calcium spike variability. The Journal of neuroscience : the official journal of the Society for Neuroscience *33*, 15848-15867.

Attwell, D., and Laughlin, S.B. (2001). An energy budget for signaling in the grey matter of the brain. Journal of cerebral blood flow and metabolism : official journal of the International Society of Cerebral Blood Flow and Metabolism *21*, 1133-1145.

Burroughs, A., Wise, A.K., Xiao, J.Q., Houghton, C., Tang, T.Y., Suh, C.Y., Lang, E.J., Apps, R., and Cerminara, N.L. (2017). The dynamic relationship between cerebellar Purkinje cell simple spikes and the spikelet number of complex spikes. J Physiol-London *595*, 283-299.

Carey, M.R., and Regehr, W.G. (2009). Noradrenergic control of associative synaptic plasticity by selective modulation of instructive signals. Neuron *62*, 112-122.

Carnevale, N.T., and Hines, M.L. (2006). The NEURON book (Cambridge, UK ; New York: Cambridge University Press).

Carter, B.C., and Bean, B.P. (2009). Sodium entry during action potentials of mammalian neurons: incomplete inactivation and reduced metabolic efficiency in fast-spiking neurons. Neuron *64*, 898-909.

Carter, B.C., and Bean, B.P. (2011). Incomplete inactivation and rapid recovery of voltage-dependent sodium channels during high-frequency firing in cerebellar Purkinje neurons. Journal of neurophysiology *105*, 860-871.

Cichon, J., and Gan, W.B. (2015). Branch-specific dendritic Ca(2+) spikes cause persistent synaptic plasticity. Nature *520*, 180-185.

Coesmans, M., Weber, J.T., De Zeeuw, C.I., and Hansel, C. (2004). Bidirectional parallel fiber plasticity in the cerebellum under climbing fiber control. Neuron *44*, 691-700.

Davie, J.T., Clark, B.A., and Hausser, M. (2008). The origin of the complex spike in cerebellar Purkinje cells. The Journal of neuroscience : the official journal of the Society for Neuroscience *28*, 7599-7609.

De Schutter, E., and Bower, J.M. (1994a). An active membrane model of the cerebellar Purkinje cell II. Simulation of synaptic responses. Journal of neurophysiology *71*, 401-419.

De Schutter, E., and Bower, J.M. (1994b). An active membrane model of the cerebellar Purkinje cell. I. Simulation of current clamps in slice. Journal of neurophysiology *71*, 375-400.

Deneux, T., Kaszas, A., Szalay, G., Katona, G., Lakner, T., Grinvald, A., Rozsa, B., and Vanzetta, I. (2016). Accurate spike estimation from noisy calcium signals for ultrafast three-dimensional imaging of large neuronal populations in vivo. Nature communications *7*, 12190.

Eccles, J.C. (1977). An instruction-selection theory of learning in the cerebellar cortex. Brain research *127*, 327-352.

Gilbert, P.F. (1976). Simple spike frequency and the number of secondary spikes in the complex spike of the cerebellar Purkinje cell. Brain research *114*, 334-338.

Golding, N.L., Staff, N.P., and Spruston, N. (2002). Dendritic spikes as a mechanism for cooperative long-term potentiation. Nature *418*, 326-331.

Hines, M.L., and Carnevale, N.T. (1997). The NEURON simulation environment. Neural computation *9*, 1179-1209.

Ito, M. (1972). Neural design of the cerebellar motor control system. Brain research *40*, 81-84.

Jelitai, M., Puggioni, P., Ishikawa, T., Rinaldi, A., and Duguid, I. (2016). Dendritic excitation-inhibition balance shapes cerebellar output during motor behaviour. Nature communications *7*, 13722.

Keren, N., Peled, N., and Korngreen, A. (2005). Constraining compartmental models using multiple voltage recordings and genetic algorithms. Journal of neurophysiology *94*, 3730-3742.

Khaliq, Z.M., Gouwens, N.W., and Raman, I.M. (2003). The contribution of resurgent sodium current to high-frequency firing in Purkinje neurons: an experimental and modeling study. The Journal of neuroscience : the official journal of the Society for Neuroscience *23*, 4899-4912.

Khaliq, Z.M., and Raman, I.M. (2005). Axonal propagation of simple and complex spikes in cerebellar Purkinje neurons. The Journal of neuroscience : the official journal of the Society for Neuroscience *25*, 454-463.

Khavandgar, S., Walter, J.T., Sageser, K., and Khodakhah, K. (2005). Kv1 channels selectively prevent dendritic hyperexcitability in rat Purkinje cells. The Journal of physiology *569*, 545-557.

Kitamura, K., and Hausser, M. (2011). Dendritic calcium signaling triggered by spontaneous and sensory-evoked climbing fiber input to cerebellar Purkinje cells in vivo. The Journal of neuroscience : the official journal of the Society for Neuroscience *31*, 10847-10858.

Larkum, M.E., Zhu, J.J., and Sakmann, B. (2001). Dendritic mechanisms underlying the coupling of the dendritic with the axonal action potential initiation zone of adult rat layer 5 pyramidal neurons. The Journal of physiology *533*, 447-466.

Lev-Ram, V., Wong, S.T., Storm, D.R., and Tsien, R.Y. (2002). A new form of cerebellar long-term potentiation is postsynaptic and depends on nitric oxide

but not cAMP. Proceedings of the National Academy of Sciences of the United States of America *99*, 8389-8393.
Mano, N. (1970). Changes of simple and complex spike activity of cerebellar purkinje cells with sleep and waking. Science *170*, 1325-1327.
Marr, D. (1969). A theory of cerebellar cortex. The Journal of physiology *202*, 437-470.
Martina, M., Metz, A.E., and Bean, B.P. (2007). Voltage-dependent potassium currents during fast spikes of rat cerebellar Purkinje neurons: inhibition by BDS-I toxin. Journal of neurophysiology *97*, 563-571.
Martina, M., Yao, G.L., and Bean, B.P. (2003). Properties and functional role of voltage-dependent potassium channels in dendrites of rat cerebellar Purkinje neurons. The Journal of neuroscience : the official journal of the Society for Neuroscience *23*, 5698-5707.
Maruta, J., Hensbroek, R.A., and Simpson, J.I. (2007). Intraburst and interburst signaling by climbing fibers. The Journal of neuroscience : the official journal of the Society for Neuroscience *27*, 11263-11270.
Masoli, S., Solinas, S., and D'Angelo, E. (2015). Action potential processing in a detailed Purkinje cell model reveals a critical role for axonal compartmentalization. Front Cell Neurosci *9*, 47.
Mathy, A., Ho, S.S., Davie, J.T., Duguid, I.C., Clark, B.A., and Hausser, M. (2009). Encoding of oscillations by axonal bursts in inferior olive neurons. Neuron *62*, 388-399.
Najafi, F., Giovannucci, A., Wang, S.S., and Medina, J.F. (2014). Coding of stimulus strength via analog calcium signals in Purkinje cell dendrites of awake mice. eLife *3*, e03663.
Ohtsuki, G., Piochon, C., Adelman, J.P., and Hansel, C. (2012). SK2 channel modulation contributes to compartment-specific dendritic plasticity in cerebellar Purkinje cells. Neuron *75*, 108-120.
Otsu, Y., Marcaggi, P., Feltz, A., Isope, P., Kollo, M., Nusser, Z., Mathieu, B., Kano, M., Tsujita, M., Sakimura, K.*, et al.* (2014). Activity-dependent gating of calcium spikes by A-type K+ channels controls climbing fiber signaling in Purkinje cell dendrites. Neuron *84*, 137-151.
Palmer, L.M., Clark, B.A., Grundemann, J., Roth, A., Stuart, G.J., and Hausser, M. (2010). Initiation of simple and complex spikes in cerebellar Purkinje cells. The Journal of physiology *588*, 1709-1717.
Piochon, C., Titley, H.K., Simmons, D.H., Grasselli, G., Elgersma, Y., and Hansel, C. (2016). Calcium threshold shift enables frequency-independent control of plasticity by an instructive signal. Proceedings of the National Academy of Sciences of the United States of America *113*, 13221-13226.
Roth, A., and Hausser, M. (2001). Compartmental models of rat cerebellar Purkinje cells based on simultaneous somatic and dendritic patch-clamp recordings. The Journal of physiology *535*, 445-472.
Schmolesky, M.T., Weber, J.T., De Zeeuw, C.I., and Hansel, C. (2002). The making of a complex spike: ionic composition and plasticity. Annals of the New York Academy of Sciences *978*, 359-390.
Steuber, V., Mittmann, W., Hoebeek, F.E., Silver, R.A., De Zeeuw, C.I., Hausser, M., and De Schutter, E. (2007). Cerebellar LTD and pattern recognition by Purkinje cells. Neuron *54*, 121-136.

726 Swensen, A.M., and Bean, B.P. (2003). Ionic mechanisms of burst firing in
727 dissociated Purkinje neurons. The Journal of neuroscience : the official journal of
728 the Society for Neuroscience *23*, 9650-9663.
729 Warnaar, P., Couto, J., Negrello, M., Junker, M., Smilgin, A., Ignashchenkova, A.,
730 Giugliano, M., Thier, P., and De Schutter, E. (2015). Duration of Purkinje cell
731 complex spikes increases with their firing frequency. Front Cell Neurosci *9*.
732 Wilms, C.D., and Hausser, M. (2015). Reading out a spatiotemporal population
733 code by imaging neighbouring parallel fibre axons in vivo. Nature
734 communications *6*, 6464.
735 Yang, Y., and Lisberger, S.G. (2014). Purkinje-cell plasticity and cerebellar motor
736 learning are graded by complex-spike duration. Nature *510*, 529-532.
737 Zagha, E., Manita, S., Ross, W.N., and Rudy, B. (2010). Dendritic Kv3.3 potassium
738 channels in cerebellar purkinje cells regulate generation and spatial dynamics of
739 dendritic Ca2+ spikes. Journal of neurophysiology *103*, 3516-3525.
740
741

Supplementary Information

Supplementary Figures

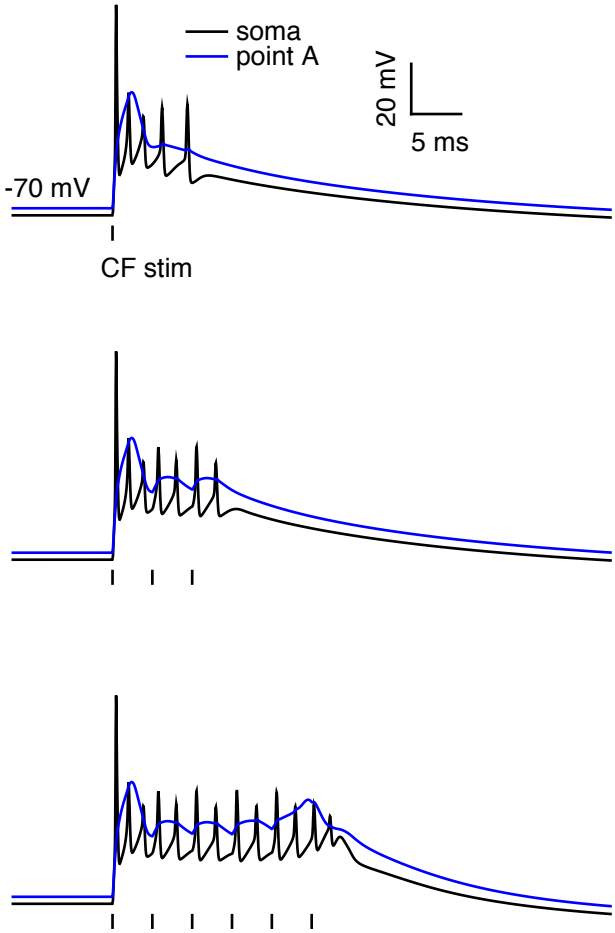

Figure S1. PC responses to CF bursts.
We reproduced the experiment by Mathy et al. (2009). Example somatic and dendritic responses to CF burst with 1 (up), 3 (middle) and 6 spikes (bottom) in the CF burst. The simulated instantaneous CF bursting frequency is 250 Hz close to the experimentally reported ~ 273 Hz.

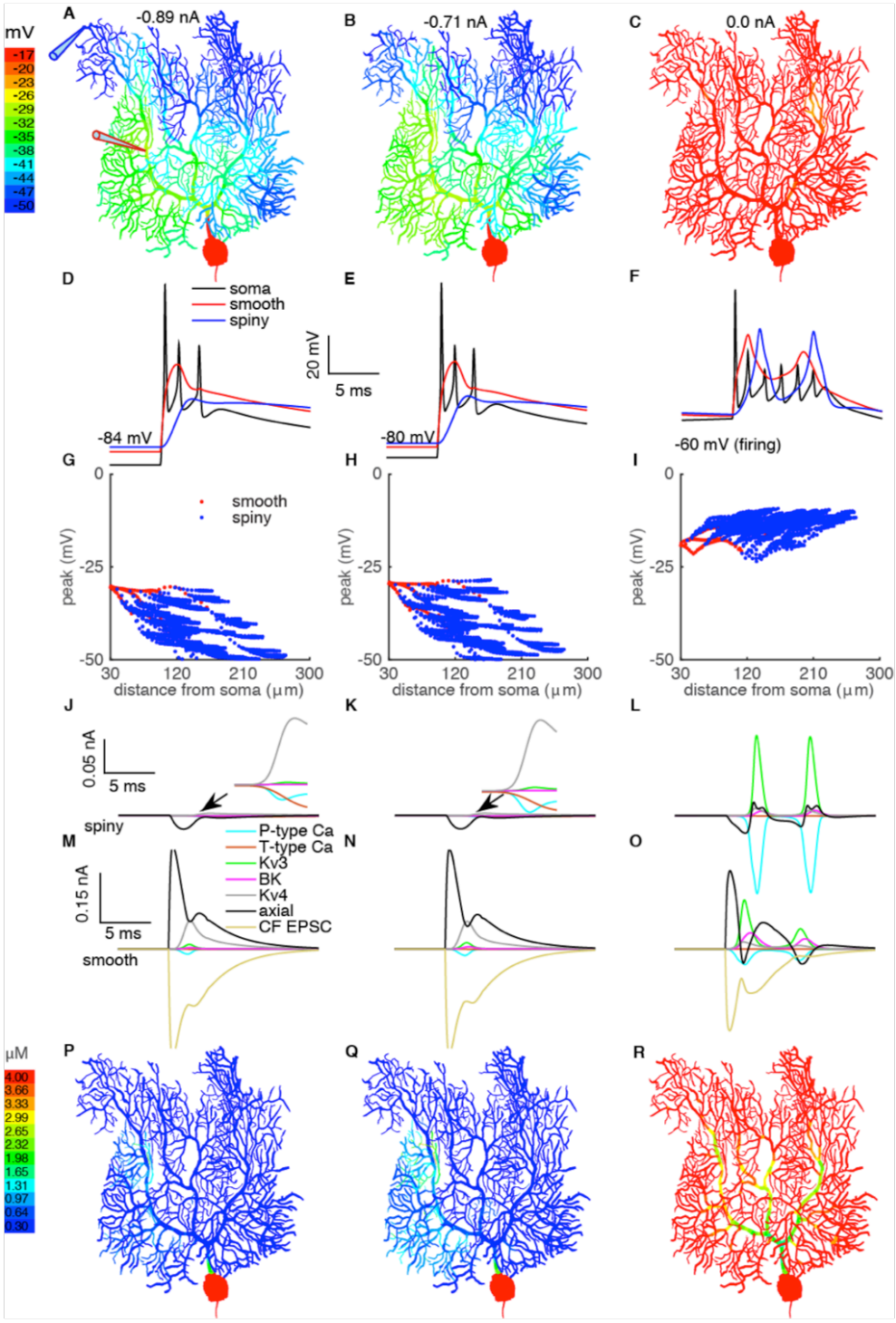

Figure S2. Voltage states regulate CF-evoked dendritic spike generation and propagation. **A-C.** Color-coded representation of dendritic voltage responses at different holding potentials (-84 mV, -80 mV and -60 mV respectively). **D-F.** Example somatic CSs (black), dendritic voltage responses on the smooth dendrite (red) and spiny dendrite (blue) at different voltage states. **G-I.** Distance-dependent propagation of dendritic responses at different voltage states. **J-L.** Ionic currents in the distal spiny dendritic site at different voltage states. **M-O.** Ionic currents in the proximal smooth dendritic site at different voltage states. The surface areas of the segments chosen at the smooth dendrite and spiny dendrite are 64 μm^2 and 23 μm^2 respectively. **P-R.** Color-coded peak Ca^{2+} concentrations at corresponding membrane potentials.

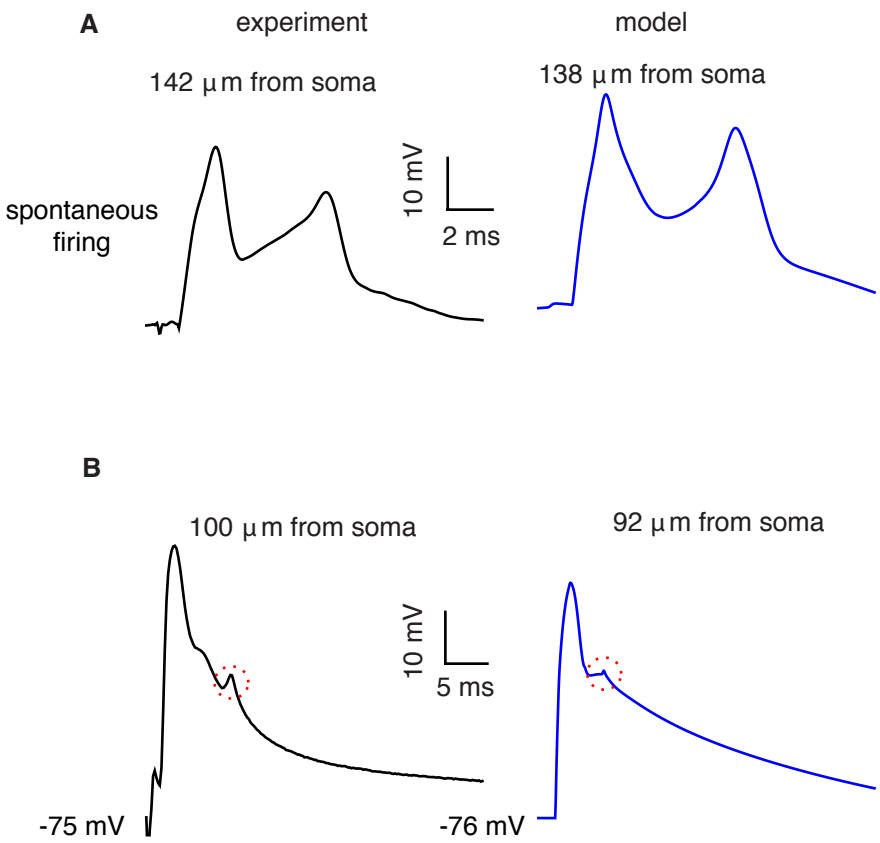

Figure S3. CF-evoked dendritic voltage response waveforms with different current injections (holding potentials).
A. CF-evoked dendritic spike with two spikelets in the experiment (left, reproduced from Fig.5A of Davie et al. (2008)) and in the model (right). **B.** CF-evoked dendritic voltage response in the experiment (left, data from Ohtsuki et al. (2012)) and in the model (right). The 'deflection' caused by a somatic Na^+ spikelet can be found on top of the dendritic response under this condition in both experimental recording and in the model (circled in the figure).

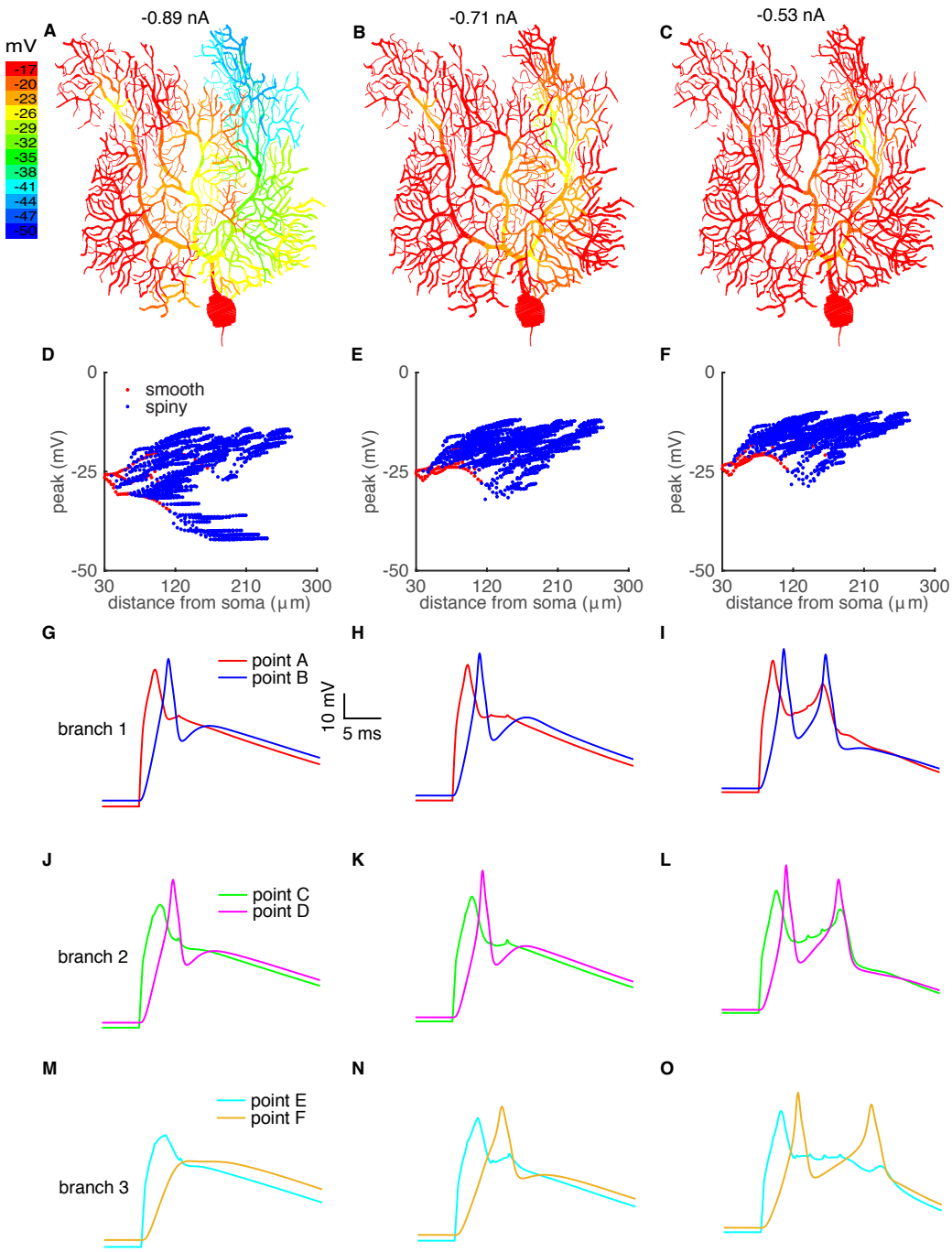

Figure S4. Global inactivation of the Kv4 current can facilitate the occurrence of dendritic spikes and make the dendritic excitability more homogenous.
The Kv4 inactivation was simulated by left shifting its availability by 11 mV. Dendritic responses to holding currents of -0.89 nA, -0.71 nA and -0.53 nA are shown from left to right. Color-coded representation of dendritic response peaks, distance-dependent propagation of dendritic response peaks, and dendritic responses (EPSP or spike) at different branches are shown from top to bottom.

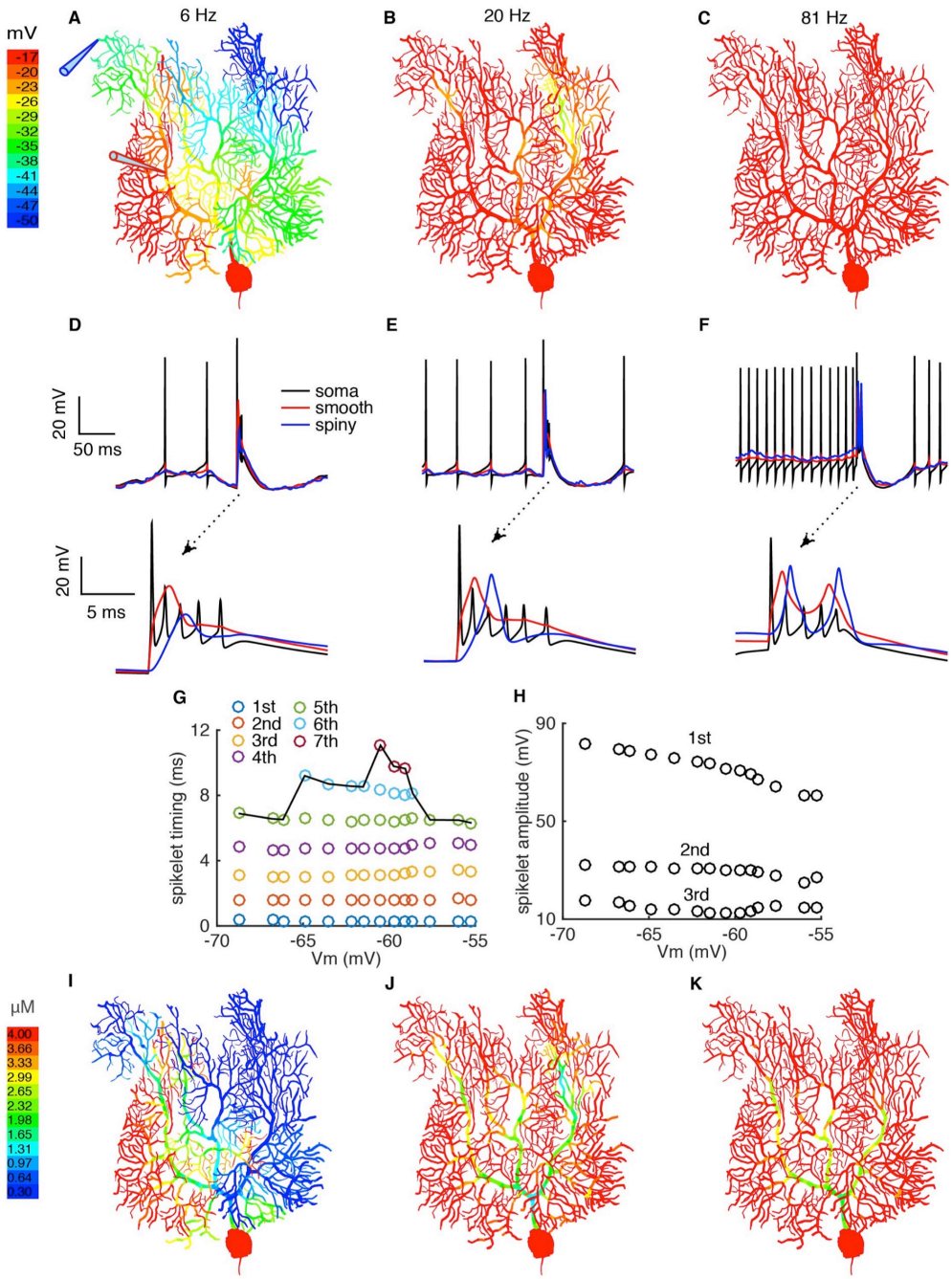

Figure S5. CF responses when the voltage states of the PC are manipulated by combined excitatory and inhibitory synaptic inputs.
A-C show color-coded representation of dendritic voltage response peaks with the increase of SSFRs. **D-F** show the corresponding example somatic and dendritic responses. CF responses at a higher time scale are shown in the bottom panel. **G** shows the effect of somatic voltage states on the CS spikelet numbers and durations. **H.** Effect of somatic voltage states on the amplitudes of the first 3 somatic spikelets. **I-K** show color-coded CF-evoked peak Ca^{2+} concentrations with the corresponding SSFR.

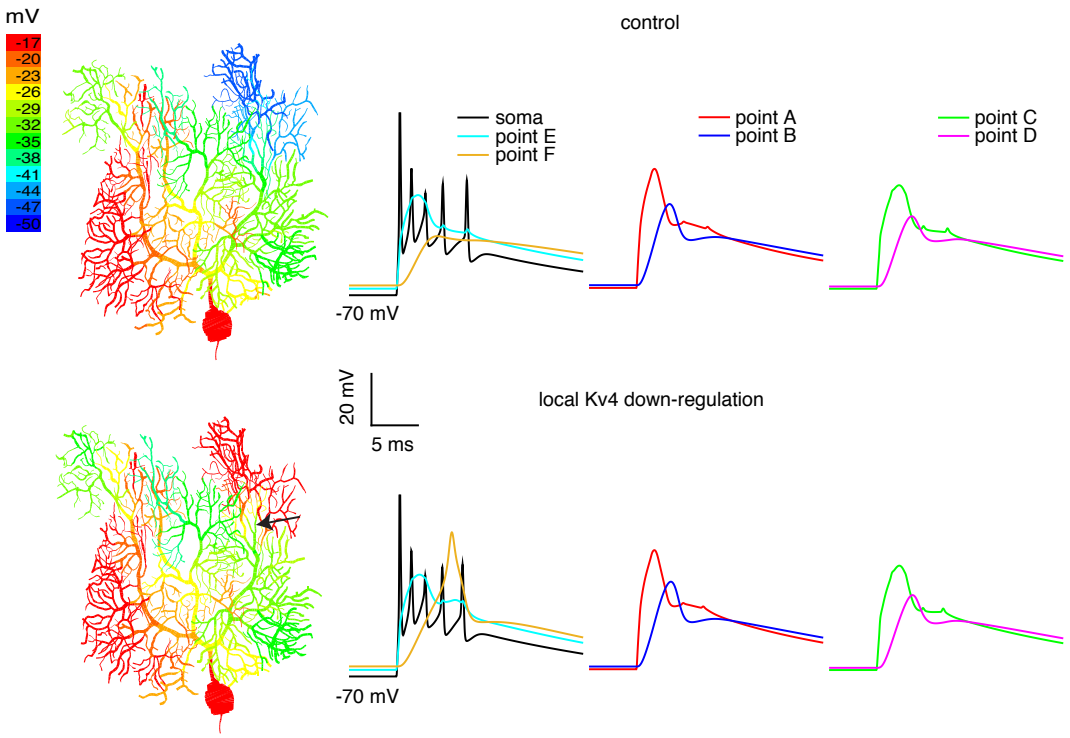

Figure S6. Local down-regulation of Kv4 current mdulates dendritic responses in a spatially precise manner.
In the child branchlet of the labeled dendritic section, the availability of Kv4 current is left shifted by 11 mV (bottom panel). Only the dendritic responses located within the labeled branchlet (For example, Point F) are facilitated by the local Kv4 down-regulation. In other parts of the dendrite, dendritic responses are not affected.

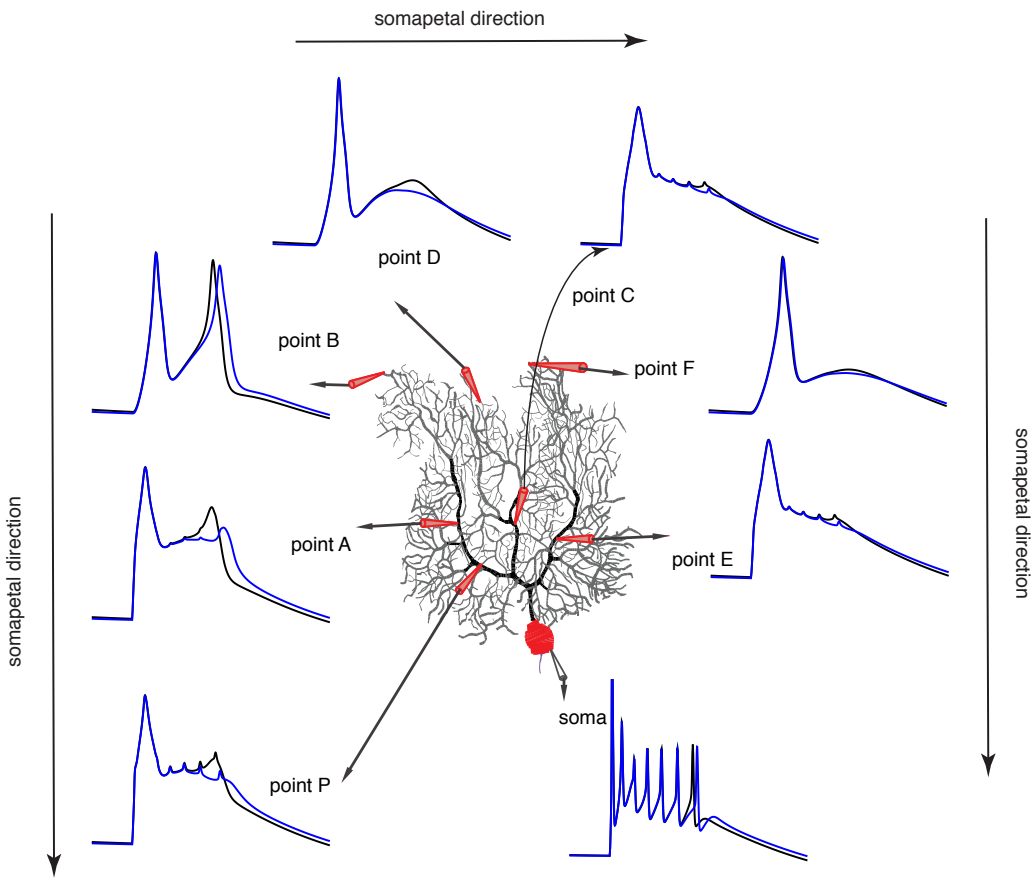

Figure S7. The dendritic spike measured on the proximal smooth dendrite can't reflect dendritic responses in the rest of the dendrite.
Here we reproduce the experiment by Davie et al. (2008). The holding current is -0.2 nA. The CF is activated at different phases of the somatic interspike interval to achieve a slight change of dendritic voltage state. In case I (blue traces), a secondary dendritic spikelet occurs at point B of the distal dendrite. However, at point A and P of the same branch closer to the soma, no secondary dendritic spikelets are triggered. With a slight depolarization of the dendrite in case II (black traces), secondary dendritic spikelets occur at both proximal sites (point A and point P) and at the distal site (point B).

Supplementary Experimental Procedures

Current equations and calcium handling

1) Na^+ current in the PC.

Na^+ current in the model is distributed in the AIS and soma. Na^+ current in the PC is composed of 'transient', 'persistent' and 'resurgent' components. We started from the previous model (Khaliq et al., 2003) and made slight changes (Narsg). In the soma, we adjusted the reaction rates between the I1 - I5 states by right shifting 5 mV (Yan et al., 2014): $\alpha = 150\, e^{(V-5)/20}$, $\beta = 3\, e^{(V-5)/-20}$. Other parameters are the same as the original model. This adjustment mainly right-shifts the inactivation curve of this current by ~ 2.5 mV. The inactivation curve of the modified model lies within measurements (Raman and Bean, 2001; Yan et al., 2014). In the AIS, beside the above-mentioned adjustment, we also adjusted deactivation rates between C1 - C5 to lower the spike threshold in the AIS, as done by Colbert and Pan (2002). Therefore, $\beta = 3\, e^{(V+15)/-15}$ for reaction rates between C1 - C5. First, by this adjustment, the contribution of AIS spikes to somatic spikes is closer to measured data (represented by d^2V/dt^2 in Fig. 1D). Second, we removed the frequently failed recovery of simple spikes after a complex spike when there is no obvious after-hyperpolarization following the complex spike (although this can be observed in some experiments, data shared by Paul Mathews from UCLA).

It is impossible to approximate Na^+ currents using a single model, given their multiple components. In the original model (Khaliq et al., 2003), the persistent component is tiny. Therefore, we incorporated an additional persistent Na^+ current model to compensate (NaP). The steady state activation curve is from Carter et al. (2012), $m_{ss} = 1/(1 + e^{-(V+66)/5})$. The time constant is from Baker (2005), $\tau_m = 1/(\alpha_m + \beta_m)$, $\alpha_m = 1/(\,17.235/(1+e^{(V+27.58)/-11.47}\,))$, $\beta_m = 1/(\,17.235/(1+e^{(V+86.2)/19.8}\,))$. This persistent component helps to maintain spike firing during negative current injections.

2) H-current in the PC

H-current (Ih) is distributed in the whole PC (Angelo et al., 2007). In our model, the formulations are the same as the model formulations from Angelo et al. (2007), except we shifted the activation curve to a more hyperpolarized direction by 6 mV to make 'sag' responses with different holding currents more comparable to experimental recordings (Fig. 1G).

3) T-type Ca^{2+} current in the PC

T-type Ca^{2+} current is distributed in the AIS (Bender and Trussell, 2009), the smooth dendrite and the spiny dendrite (Hildebrand et al., 2009; Otsu et al., 2014). The formulation of this current is according to data from Otsu et al. (2014). $m_{ss} = 1/(1 + e^{-(V-35.606)/4.7})$, $\tau_m = 1/(1.2757 + \alpha_m + \beta_m)$, $\alpha_m = -2.3199/(1 + e^{(V+41.448)/-30.655})$, $\beta_m = 2.5712/(1 + e^{(V+21.7866)/-9.6306})$, $h_{ss} = 1/(1 + e^{(V+81.718)/6.4635})$, $\tau_h = 1/(0.0076 + \alpha_h + \beta_h)$, $\alpha_h = 0.17746/(1 + e^{(V+41.448)/-30.655})$, $\beta_h = 0.13402/(1 + e^{(V+94.836)/-5.5845})$. In the model, both BK and SK2 don't sense Ca^{2+} influx from T-type Ca^{2+} channels.

4) P-type Ca^{2+} current in the PC

P-type Ca^{2+} current is distributed throughout the entire PC (Indriati et al., 2013). The formulation of this current is according to the data fromBenton and Raman (2009). $m_{ss} = 1/(1 + e^{-(V-25.5)/4.113})$, $\tau_m = 0.2 + 0.7031e^{-((V+25)/14)^2}$.

5) Ca^{2+} handling mechanism

In the dendrite, we used the formulation from Anwar et al. (2012) with 4 shells. In both soma and AIS, we made BK channels sense Ca^{2+} signals closer to the membrane surface (subspace) or Ca^{2+} channels by increasing the number of shells (Indriati et al., 2013). In the AIS, we still used the formulation as in Anwar et al. (2012), but we increased the number of shells to 10. In the soma, we used the fixed depth scheme for the outermost shell and 20 shells in total to reduce the computational load (Anwar et al., 2014). We also incorporated a sarcoplasmic endoplasmic reticulum Ca^{2+}ATPase (SERCA) pump to reduce the spike-over-spike Ca^{2+} summation in AIS and soma. $J_{SERCA} = 0.1 * vol(i) * Ca[i]/(Ca[i] + 0.0058(mM))$, $vol(i)$ means the volume of the i_{th} shell. $Ca[i]$ means the free Ca^{2+} concentration of the i_{th} shell.

6) BK current in the PC

We used the same formulation from Anwar et al. (2012) as the fast (or IBTX-sensitive) component of the BK current (Benton et al., 2013). We also incorporated the slow (or IBTX-insensitive) component of BK current (Benton et al., 2013) from Jaffe et al. (2011). The formulation of their type II model was used. The fast component is distributed in the whole PC and the slow component is only distributed in the soma and the AIS.

7) SK2 current in the PC

SK2 current is distributed in the whole PC (Belmeguenai et al., 2010; Swensen and Bean, 2003). We used the formulation from Solinas et al. (2007) according to the data by Hirschberg et al. (1998).

8) Kv3 current in the PC

KV3 current is distributed in the whole PC (Martina et al., 2003). The formulation is from Akemann et al. (2009) according to the data from Martina et al. (2007). In our model, the steady state activation curve is left shifted by 4 mV with $V_{0.5} \approx 2$ mV, which is still within the experimental range (Martina et al., 2007; Martina et al., 2003; Zagha et al., 2010).

9) Kv4 current in the PC

In our model, Kv4 current has both fast and slow inactivation components and is distributed in the smooth and the spiny dendrites (Otsu et al., 2014). We took the steady state activation curve from Gunay et al. (2008). The inactivation curve and time constants are according to experimental data of Stéphane Dieudonné. $m_{ss} = 1/(1 + e^{(V+49)/-12.5})$, $\tau_m = 1/(\alpha_m + \beta_m)$, $\alpha_m = 0.1342/(1 + e^{(V+60)/32.19976})$, $\beta_m = 0.15743/(1 + e^{(V+57)/37.51346})$, $h_{ss} = 1/(1 + e^{(V+75.30348)/6.06329})$, $\tau_{hf} = 1/(\alpha_{hf} + \beta_{hf})$, $\alpha_{hf} = 0.01342/(1 + e^{(V+60)/7.86476})$, $\beta_{hf} = 0.04477/(1 + e^{(V+54)/-11.6315})$, $\tau_{hs} = 100$.

10) Kv1 current in the PC

In our model, Kv1 is distributed in the dendrite (Khavandgar et al., 2005). The formulation is from Akemann and Knopfel (2006). We added an inactivation gate,

904 according to data from Otsu et al. (2014). $h_{ss} = 1/(1 + e^{(V+66.16)/6.1881})$. Due to the
905 slow inactivation process, the inactivation time constant was set to be 1000 ms.
906
907 **Parameter tuning**
908 The model was hand-tuned because extensive preceding efforts using automatic
909 parameter searching did not achieve good results (Achard and De Schutter, 2006; Van
910 Geit et al., 2007). Due to technical limitations, we can only get simultaneous somatic
911 and dendritic patch-clamp recordings (single dendritic site) to constrain the model in
912 most cases. However, it has been demonstrated that data recorded from just two
913 locations in the same L5 pyramidal neuron are not sufficient to accurately constrain a
914 compartmental model (Keren et al., 2005). For the PC, we were able to get good F-I
915 curves and 'sag' responses with automated search methods, but the dendrite model
916 could not generate physiologic responses. This is because we don't have sufficient
917 data to constrain the active properties of the dendrite and the interaction between
918 soma and dendrite by automatic parameter searching. Therefore, we decided to use
919 hand-tuning instead, and we tried to incorporate as many experimental observations
920 as possible into the model. After repeated modification over a period of more than
921 two years, we achieved the present model.
922
923 1) Currents in the soma
924 The Na^+ current profile nearly coincides with the total net ionic current during the
925 depolarization phase of dissociated PC AP-clamp recordings (Carter and Bean, 2009).
926 The total net ionic current is calculated by –C*dV/dt, where C is the cell capacitance
927 and dV/dt is the time derivative of the voltage. The results of Carter and Bean suggest
928 that Na^+ current is nearly the sole current supporting the depolarization and K^+
929 currents are not activated during the depolarization phase (as illustrated in Fig. 2 of
930 their paper). This also agrees with the high activation threshold of K^+ currents in the
931 PC (Martina et al., 2007). This finding provided an opportunity to firmly constrain the
932 somatic ionic currents. The measured peak Na^+ current amplitude is 12.5 nA in
933 dissociated mouse PCs with a capacitance of 12 pF, but the ratio of
934 current/capacitance in the soma may be underestimated due to the possible remaining
935 stump of the dendritic tree. In our model, we have a peak somatic Na^+ current of 17
936 nA relative to a capacitance of 10.5 pF in the soma. Then we fixed the conductance
937 density of somatic Kv3 current by constraining the spike half-amplitude duration
938 (0.15 ms) close to experimental measurements (0.17 ms, we also gave consideration
939 to the spike duration in the intact PC as shown in Fig. 1B). The high activation
940 threshold of the Kv3 current makes it active mainly during the repolarization phase
941 (Carter and Bean, 2009) and constrains the spike duration (Martina et al., 2007).
942 Subsequently, we constrained the conductance density of P-type Ca^{2+} current and BK
943 current to have an AHP (-77 mV) comparable to the recorded (-82 mV, still we also
944 considered the AHP in the intact PC ~ -70 mV). The conductance density of P-type
945 Ca^{2+} is constrained to be the same as that in the smooth dendrite. Then only SK2 and
946 Ih remained unconstrained for the somatic ionic currents. We initially assigned
947 tentative conductance density values for these two currents to develop a firing somata
948 model (like the previous Kaliq-Raman model (Khaliq et al., 2003)). To reflect the
949 negligible role of Ih in dissociated PC firing (Raman and Bean, 1999), the
950 conductance density of Ih is half of that in smooth dendrite. In the intact PC, the
951 conductance density of somatic SK2 current is adjusted to get a F-I curve close to the
952 experimental measurements (Fig. 1G). The persistent component of Na^+ current is

953 constrained so that the intact PC still fires with -0.17 nA somatic holding current, but
954 it stops firing when the current amplitude changes to -0.36 nA.
955
956 2) Currents in the AIS
957 We constrained ionic currents in the AIS to make the model behave like experimental
958 data in two aspects: the axosomatic delay of the simple spike (Fig. 1B) and the second
959 derivative of the simple spike (Fig. 1D). The first reflects how the spike in the AIS
960 precedes the somatic spike and the second reflects the contribution of the spike in the
961 AIS to the somatic spike. We assumed the conductance densities of Ih in AIS are the
962 same as in soma.
963
964 3) Currents in the dendrite
965 Due to the limited quantitative data, currents in the dendrite are more difficult to
966 constrain compared with somatic currents. We first constrained the P-type Ca^{2+}
967 current in the dendrite. In the spiny dendrite, Ca^{2+} influx during one dendritic spikelet
968 is 1.3e-14 C/μm^3 in our model, which is close to the experimentally estimated 1.1e-14
969 C/μm^3 (Otsu et al., 2014). The CF-evoked Ca^{2+} influx increases with distance from
970 soma when a Ca^{2+}-supported dendritic spike occurs (Kitamura and Hausser, 2011;
971 Otsu et al., 2014). Therefore, in the smooth dendrite, the current density was
972 constrained to have a calcium influx ratio (smooth dendrite relative to the spiny
973 dendrite at same membrane surface area) of 0.36. The conductance densities of P-type
974 Ca^{2+} current are further supported by the time to peak of the first dendritic spikelet
975 being ~ 1.5 ms in the smooth dendrite (Davie et al., 2008; Kitamura and Hausser,
976 2011). Conductance densities of Kv4 current are assumed to be homogeneously
977 distributed and then repeatedly adjusted to make this current able to 'brake' the
978 dendritic spikes at low voltage ranges. We distribute more T-type Ca^{2+} channels
979 (Hildebrand et al., 2009) in the spiny dendrite given they are preferentially distributed
980 on spines. This current helps to offset the window current of Kv4 current to maintain
981 the dendritic interspike interval membrane potential. We distribute larger conductance
982 densities of BK current on the smooth dendrite compared to on spiny dendrite, given
983 the BK channel clusters are mainly distributed on the soma and smooth dendrite
984 (Kaufmann et al., 2010). BK current contributes to reasonable AHP after complex
985 spikes as found in Davie et al. (2008). Ih is constrained to get a 'sag' response close to
986 the experimental recordings (Fig. 1G). Kv1 and SK2 help to regulate dendritic
987 excitability to stop the occurrence of Na^+-Ca^{2+} bursting at low current injections. In
988 our model, as with most cell recordings in rat PCs, Na^+-Ca^{2+} bursts begin to occur
989 with 1.25 nA somatic current injection. In addition, this dendrite model can replicate
990 the distance-dependent decay of the simple spike amplitude (Fig. 1E), the regulatory
991 role of Kv4 current in voltage-dependent dendritic spike generation and propagation
992 (Fig. 3,S2,S5), dendritic voltage response waveforms at different conditions (Fig. S3),
993 and peak dendritic voltage response propagation with distance from the soma at
994 specific condition (Fig. 3G).
995
996
997 **Current conductance densities in different part of PC**
998

Currents (nS/cm²)	AIS	soma	smooth dendrite	spiny dendrite
Narsg	0.56	0.0317	0	0
NaP	0.0023	1.4e-4	0	0

Ih	1.08e-4	1.08e-4	2.16e-4	3.24e-4
T- type Ca^{2+}	1.28e-4	0	2.7e-5	1.08e-4
P-type Ca^{2+}	1.05	1.9e-4	1.9e-4	7.6e-4
BKfast	6	0.8736	0.21	0.0448
BKslow	1.05	0.3	0	0
SK2	0.0278	0.0075	2.16e-4	3.6e-4
Kv3	115	1.8	0.1512	0.2268
Kv4	0	0	0.015	0.015
Kv1	0	0	0.002	0.001

Supplementary References

Achard, P., and De Schutter, E. (2006). Complex parameter landscape for a complex neuron model. PLoS computational biology *2*, e94.

Akemann, W., and Knopfel, T. (2006). Interaction of Kv3 potassium channels and resurgent sodium current influences the rate of spontaneous firing of Purkinje neurons. The Journal of neuroscience : the official journal of the Society for Neuroscience *26*, 4602-4612.

Akemann, W., Lundby, A., Mutoh, H., and Knopfel, T. (2009). Effect of voltage sensitive fluorescent proteins on neuronal excitability. Biophysical journal *96*, 3959-3976.

Angelo, K., London, M., Christensen, S.R., and Hausser, M. (2007). Local and global effects of I(h) distribution in dendrites of mammalian neurons. The Journal of neuroscience : the official journal of the Society for Neuroscience *27*, 8643-8653.

Anwar, H., Hong, S., and De Schutter, E. (2012). Controlling Ca2+-activated K+ channels with models of Ca2+ buffering in Purkinje cells. Cerebellum *11*, 681-693.

Anwar, H., Roome, C.J., Nedelescu, H., Chen, W., Kuhn, B., and De Schutter, E. (2014). Dendritic diameters affect the spatial variability of intracellular calcium dynamics in computer models. Front Cell Neurosci *8*, 168.

Baker, M.D. (2005). Protein kinase C mediates up-regulation of tetrodotoxin-resistant, persistent Na+ current in rat and mouse sensory neurones. The Journal of physiology *567*, 851-867.

Belmeguenai, A., Hosy, E., Bengtsson, F., Pedroarena, C.M., Piochon, C., Teuling, E., He, Q., Ohtsuki, G., De Jeu, M.T., Elgersma, Y.*, et al.* (2010). Intrinsic plasticity complements long-term potentiation in parallel fiber input gain control in cerebellar Purkinje cells. The Journal of neuroscience : the official journal of the Society for Neuroscience *30*, 13630-13643.

Bender, K.J., and Trussell, L.O. (2009). Axon initial segment Ca2+ channels influence action potential generation and timing. Neuron *61*, 259-271.

Benton, M.D., Lewis, A.H., Bant, J.S., and Raman, I.M. (2013). Iberiotoxin-sensitive and -insensitive BK currents in Purkinje neuron somata. Journal of neurophysiology *109*, 2528-2541.

Benton, M.D., and Raman, I.M. (2009). Stabilization of Ca current in Purkinje neurons during high-frequency firing by a balance of Ca-dependent facilitation and inactivation. Channels *3*, 393-401.

1038 Carter, B.C., and Bean, B.P. (2009). Sodium entry during action potentials of
1039 mammalian neurons: incomplete inactivation and reduced metabolic efficiency
1040 in fast-spiking neurons. Neuron *64*, 898-909.
1041 Carter, B.C., Giessel, A.J., Sabatini, B.L., and Bean, B.P. (2012). Transient Sodium
1042 Current at Subthreshold Voltages: Activation by EPSP Waveforms. Neuron *75*,
1043 1081-1093.
1044 Colbert, C.M., and Pan, E. (2002). Ion channel properties underlying axonal action
1045 potential initiation in pyramidal neurons. Nature neuroscience *5*, 533-538.
1046 Davie, J.T., Clark, B.A., and Hausser, M. (2008). The origin of the complex spike in
1047 cerebellar Purkinje cells. The Journal of neuroscience : the official journal of the
1048 Society for Neuroscience *28*, 7599-7609.
1049 Gunay, C., Edgerton, J.R., and Jaeger, D. (2008). Channel density distributions
1050 explain spiking variability in the globus pallidus: a combined physiology and
1051 computer simulation database approach. The Journal of neuroscience : the
1052 official journal of the Society for Neuroscience *28*, 7476-7491.
1053 Hildebrand, M.E., Isope, P., Miyazaki, T., Nakaya, T., Garcia, E., Feltz, A., Schneider,
1054 T., Hescheler, J., Kano, M., Sakimura, K.*, et al.* (2009). Functional Coupling
1055 between mGluR1 and Ca(v)3.1 T-Type Calcium Channels Contributes to Parallel
1056 Fiber-Induced Fast Calcium Signaling within Purkinje Cell Dendritic Spines.
1057 Journal of Neuroscience *29*, 9668-9682.
1058 Hirschberg, B., Maylie, J., Adelman, J.P., and Marrion, N.V. (1998). Gating of
1059 recombinant small-conductance Ca-activated K+ channels by calcium. The
1060 Journal of general physiology *111*, 565-581.
1061 Indriati, D.W., Kamasawa, N., Matsui, K., Meredith, A.L., Watanabe, M., and
1062 Shigemoto, R. (2013). Quantitative localization of Cav2.1 (P/Q-type) voltage-
1063 dependent calcium channels in Purkinje cells: somatodendritic gradient and
1064 distinct somatic coclustering with calcium-activated potassium channels. The
1065 Journal of neuroscience : the official journal of the Society for Neuroscience *33*,
1066 3668-3678.
1067 Jaffe, D.B., Wang, B., and Brenner, R. (2011). Shaping of action potentials by type I
1068 and type II large-conductance Ca(2)+-activated K+ channels. Neuroscience *192*,
1069 205-218.
1070 Kaufmann, W.A., Kasugai, Y., Ferraguti, F., and Storm, J.F. (2010). Two distinct
1071 pools of large-conductance calcium-activated potassium channels in the somatic
1072 plasma membrane of central principal neurons. Neuroscience *169*, 974-986.
1073 Keren, N., Peled, N., and Korngreen, A. (2005). Constraining compartmental
1074 models using multiple voltage recordings and genetic algorithms. Journal of
1075 neurophysiology *94*, 3730-3742.
1076 Khaliq, Z.M., Gouwens, N.W., and Raman, I.M. (2003). The contribution of
1077 resurgent sodium current to high-frequency firing in Purkinje neurons: an
1078 experimental and modeling study. The Journal of neuroscience : the official
1079 journal of the Society for Neuroscience *23*, 4899-4912.
1080 Khavandgar, S., Walter, J.T., Sageser, K., and Khodakhah, K. (2005). Kv1 channels
1081 selectively prevent dendritic hyperexcitability in rat Purkinje cells. The Journal
1082 of physiology *569*, 545-557.
1083 Kitamura, K., and Hausser, M. (2011). Dendritic calcium signaling triggered by
1084 spontaneous and sensory-evoked climbing fiber input to cerebellar Purkinje cells
1085 in vivo. The Journal of neuroscience : the official journal of the Society for
1086 Neuroscience *31*, 10847-10858.

1087 Martina, M., Metz, A.E., and Bean, B.P. (2007). Voltage-dependent potassium
1088 currents during fast spikes of rat cerebellar Purkinje neurons: inhibition by BDS-
1089 I toxin. Journal of neurophysiology *97*, 563-571.
1090 Martina, M., Yao, G.L., and Bean, B.P. (2003). Properties and functional role of
1091 voltage-dependent potassium channels in dendrites of rat cerebellar Purkinje
1092 neurons. The Journal of neuroscience : the official journal of the Society for
1093 Neuroscience *23*, 5698-5707.
1094 Otsu, Y., Marcaggi, P., Feltz, A., Isope, P., Kollo, M., Nusser, Z., Mathieu, B., Kano,
1095 M., Tsujita, M., Sakimura, K.*, et al.* (2014). Activity-dependent gating of calcium
1096 spikes by A-type K+ channels controls climbing fiber signaling in Purkinje cell
1097 dendrites. Neuron *84*, 137-151.
1098 Raman, I.M., and Bean, B.P. (1999). Ionic currents underlying spontaneous action
1099 potentials in isolated cerebellar Purkinje neurons. The Journal of neuroscience :
1100 the official journal of the Society for Neuroscience *19*, 1663-1674.
1101 Raman, I.M., and Bean, B.P. (2001). Inactivation and recovery of sodium currents
1102 in cerebellar Purkinje neurons: evidence for two mechanisms. Biophysical
1103 journal *80*, 729-737.
1104 Solinas, S., Forti, L., Cesana, E., Mapelli, J., De Schutter, E., and D'Angelo, E. (2007).
1105 Computational reconstruction of pacemaking and intrinsic
1106 electroresponsiveness in cerebellar Golgi cells. Front Cell Neurosci *1*, 2.
1107 Swensen, A.M., and Bean, B.P. (2003). Ionic mechanisms of burst firing in
1108 dissociated Purkinje neurons. The Journal of neuroscience : the official journal of
1109 the Society for Neuroscience *23*, 9650-9663.
1110 Van Geit, W., Achard, P., and De Schutter, E. (2007). Neurofitter: a parameter
1111 tuning package for a wide range of electrophysiological neuron models. Frontiers
1112 in neuroinformatics *1*, 1.
1113 Yan, H., Pablo, J.L., Wang, C., and Pitt, G.S. (2014). FGF14 modulates resurgent
1114 sodium current in mouse cerebellar Purkinje neurons. eLife *3*, e04193.
1115 Zagha, E., Manita, S., Ross, W.N., and Rudy, B. (2010). Dendritic Kv3.3 potassium
1116 channels in cerebellar purkinje cells regulate generation and spatial dynamics of
1117 dendritic Ca2+ spikes. Journal of neurophysiology *103*, 3516-3525.